



Article

A Tool for Pre-Operational Daily Mapping of Floods and Permanent Water Using Sentinel-1 Data

Luca Pulvirenti ^{1,*}, Giuseppe Squicciarino ¹, Elisabetta Fiori ¹, Luca Ferraris ¹ and Silvia Puca ²

¹ CIMA Research Foundation, I-17100 Savona, Italy; giuseppe.squicciarino@cimafoundation.org (G.S.); elisabetta.fiori@cimafoundation.org (E.F.); luca.ferraris@cimafoundation.org (L.F.)

² Italian Department of Civil Protection, Presidency of the Council of Ministers, I-00189 Rome, Italy; Silvia.Puca@protezionecivile.it

* Correspondence: luca.pulvirenti@cimafoundation.org; Tel.: +39-019-23027249

Abstract: An automated tool for pre-operational mapping of floods and inland waters using Sentinel-1 data is presented. The acronym AUTOWADE (AUTOMatic Water Areas DETector) is used to denote it. The tool provides the end user (Italian Department of Civil Protection) with a continuous, near real-time (NRT) monitoring of the extent of inland water surfaces (floodwater and permanent water). It implements the following operations: downloading of Sentinel-1 products; preprocessing of the products and storage of the resulting geocoded and calibrated data; generation of the intermediate products, such as the exclusion mask; application of a floodwater/permanent water mapping algorithm; generation of the output layer, i.e., a map of floodwater/permanent water; delivery of the output layer to the end user. The open floodwater/permanent water mapping algorithm implemented in AUTOWADE is based on a new approach, denoted as buffer-from-edge (BFE), which combines different techniques, such as clustering, edge filtering, automatic thresholding and region growing. AUTOWADE copes also with the typical presence of gaps in the flood maps caused by undetected flooded vegetation. An attempt to partially fill these gaps by analyzing vegetated areas adjacent to open water is performed by another algorithm implemented in the tool, based on the fuzzy logic. The BFE approach has been validated offline using maps produced by the Copernicus Emergency Management Service. Validation has given good results with a F1-score larger than 0.87 and a kappa coefficient larger than 0.80. The algorithm to detect flooded vegetation has been visually compared with optical data and aerial photos; its capability to fill some of the gaps present in flood maps has been confirmed.

Keywords: floods; permanent water bodies; Sentinel-1; operational applications; near real-time



Citation: Pulvirenti, L.; Squicciarino, G.; Fiori, E.; Ferraris, L.; Puca, S. A Tool for Pre-Operational Daily Mapping of Floods and Permanent Water Using Sentinel-1 Data. *Remote Sens.* **2021**, *13*, 1342. <https://doi.org/10.3390/rs13071342>

Academic Editor: Guy J.-P. Schumann

Received: 31 January 2021

Accepted: 28 March 2021

Published: 1 April 2021

Publisher's Note: MDPI stays neutral with regard to jurisdictional claims in published maps and institutional affiliations.



Copyright: © 2021 by the authors. Licensee MDPI, Basel, Switzerland. This article is an open access article distributed under the terms and conditions of the Creative Commons Attribution (CC BY) license (<https://creativecommons.org/licenses/by/4.0/>).

1. Introduction

Timely and continuous monitoring of the extent of surface water bodies is very important in the management of the living environment. On the one hand, during periods when precipitation is significantly lower than the average one, the consequent shortage of water propagates through the hydrological system and may cause drought in the different segments of the hydrological system itself, including surface water [1], whose spatial distribution represents therefore a fundamental piece of information for drought management. On the other hand, when heavy precipitation causes floods, near-real time data about floodwater extent and duration are essential to support rescue and damage recovery decisions and to facilitate rapid assessment of property loss and damage [2].

Several past studies (e.g., [3–5]) demonstrated that synthetic aperture radar (SAR) systems are suitable tools for surface water mapping. They combine a high spatial resolution (from hundreds of meters to approximately 1 m, depending on the SAR acquisition mode) with the capability, typical of microwaves, to provide data during day and night and even in the presence of cloud cover. Moreover, there is a clear physical mechanism for radar scattering from water, that is, specular reflection [6]. Unless strong wind is blowing above

the water surface, the latter has a very low roughness, and most of the incident radar energy is scattered towards the specular direction. Therefore, a water surface is generally characterized by a low backscattering and appears dark in a SAR image. Conversely, the rough non-flooded terrain exhibits a higher backscattering and a brighter image tone [7], because it scatters the radar signal in many different directions, included the backscattering one.

Specular reflection is not always the prevailing effect of the radar scattering from water. In urban and agricultural flooded areas (if plants emerge from water), a dihedral effect involving water surface and vertical structures such as stems, shrubs, or walls can take place, producing an increase of the backscattering. However, several unknowns (e.g., structure and geometry for vegetation, or height and orientation of buildings for urban areas) influence the radar response from these targets [8]. Consequently, although new insights were provided on detecting inundations in agricultural areas [9–13] and urban settlements [8,14–17], this task is still very challenging. Not only missed detections (i.e., omission errors), but also commission errors may occur when mapping surface water. In areas with complex topography, the shadowing effect strongly influences the radiometry of SAR data and produces a low backscatter that can be confused with the backscatter from water bodies. Low backscatter values are measured by SAR even in the presence of heavy precipitation (especially when dealing with X-band data) and wet snow [18–21]. Furthermore, very smooth surfaces like asphalt (roads, airports, parking lots) and/or very dry areas like deserts appear dark in SAR imagery and may be misclassified as water.

Despite the challenges previously discussed, many processing algorithms have been proposed for mapping permanent water and floodwater using SAR data in a fully automated way (e.g., [11,17,22–26]). Therefore, this application can be considered mature for operational/pre-operational implementation, at least for what concerns open water. Currently, the Copernicus Emergency Management Service (CEMS) uses satellite imagery to rapidly provide geospatial information about natural disasters. Regarding floods, SAR data are very often used by CEMS for mapping purposes to overcome the limits of optical data related to the presence of clouds and the impossibility to acquire data during nighttime (e.g., [27]). CEMS is available 24 h a day, 365 days-a-year, but is an on-demand service, which is triggered on request by authorized users. Hence, an automatic tool enabling continuous and systematic monitoring of water surfaces by routinely producing medium-high resolution maps of floodwater/permanent water can complement the rapid mapping component of CEMS for what concerns flood management. In particular, it can cope with the timeliness in the availability of maps because a continuous service does not require any user activation. Moreover, it can contribute to the effectiveness of CEMS activation through a better identification of the area of interest, when images with a very high spatial resolution are required for an accurate delineation of the flood extent.

The regular acquisitions of Sentinel-1 (S1) images, performed in the framework of the Copernicus program, guarantee a continuous streaming of C-band SAR data useful to systematically produce maps of water surfaces at medium-high spatial resolution (S1 data over land have a single-look resolution of $5 \times 20 \text{ m}^2$, Section 2.1). The availability of S1 data represents therefore the driver for the implementation of the aforementioned tool. A systematic near real-time (NRT) surface water mapping service has been recently requested by the Italian Department of Civil Protection (DCP) in the framework of its competences assigned by law.

This paper presents an automatic processor, which does not need any supervision, or user intervention, that performs a systematic daily mapping of water surfaces (both floodwater and permanent water bodies) using S1 data. The acronym AUTOWADE (AUTOMATIC Water Areas DETECTOR) is used to denote this tool. AUTOWADE has been designed in the framework of the agreement between DCP and CIMA Research Foundation, which is one of the DCP competence centers. Therefore, it has been conceived to work on a national (Italian) scale. The implementation of a service for fast mapping of floods and inland waters using S1 data requires the design of a chain formed by different components. The main component is obviously water detection, but other components must be included,

like the automatic downloading of S1 images and their preprocessing to derive geocoded and calibrated data, the generation of reference and exclusion masks, and the delivery of the data to the end user. All these components must be sequentially executed in a fully automated way. Despite the large number of studies dealing with NRT water mapping, the problem of the creation of a tool that automates the various steps needed to set up a daily service based on SAR data was rarely tackled in past studies. A fully automated TerraSAR-X based flood service was developed in [25] and adapted to S1 data in [28].

Although the present release of AUTOWADE focuses on open water (i.e., open flood-water and permanent water bodies), vegetated areas close to open water that are likely inundated as well are searched for, despite the criticalities previously underlined; the objective is to, at least partially, fill the gaps typically present in flood maps due to undetected flooded vegetation. Conversely, urban areas are not considered because the related methodologies require interferometric data (e.g., [8,15,16]), whose processing requires the use of S1 orbit ephemerides data, available 20 days after the data acquisition.

The algorithms implemented in AUTOWADE use different image processing techniques. Flooded vegetation is detected through a combined use of co- and cross-polarized S1 data performed taking advantage of the fuzzy logic. Open water is mapped using a new methodology, denoted as buffer-from-edge (BFE) approach, which combines clustering, edge filtering, automatic thresholding, and region growing; it is applied to co-polarized data only. At present, a combined use of different image processing techniques such as image tiling [29], used to identify a threshold separating open water from the surrounding land, and region growing is well-established for water mapping from SAR (e.g., [18,24,26,30,31]). However, AUTOWADE works on the national scale and, for each S1 pass over Italy, it must process a number of image slices (Section 2.1) between 2 and 7, depending on the orbit. Hence, AUTOWADE does not use the approach proposed in [29] to determine the threshold, mainly because image tiling might be time-consuming. Through the BFE approach, AUTOWADE tackles the problem in a new way, taking advantage of the availability of a reference water mask to directly analyze portions of a SAR image that likely contain comparable amounts of water and non-water pixels. The open water mapping algorithm implemented in AUTOWADE has been quantitatively validated considering maps produced by the CEMS in the period 2019–2021 as a benchmark; for the method to detect flooded vegetation close to open water, a qualitative comparison with optical data and aerial photos has been carried out.

Section 2 introduces the data used by AUTOWADE, as well as the data used to validate the AUTOWADE-derived product. Section 3 describes in detail the different modules that make up AUTOWADE, with particular emphasis on the open water mapping performed through the BFE approach. Section 4 presents the results that are discussed in Section 5, while Section 6 draws the main conclusions.

2. Data

In the next sections, the data routinely processed by AUTOWADE are introduced, together with those used for validation purposes.

2.1. Sentinel-1 Data

Sentinel-1 is a two-satellite constellation whose payload is a SAR working at C band (5.4 GHz). It operates in the Interferometric Wide Swath (IWS) mode over land; in IWS mode, S1 acquires data with a 250 km swath at a spatial resolution of $5 \times 20 \text{ m}^2$ (single look). S1 products are usually made available on the Copernicus Open Access Hub (also known as Sentinel Data Hub System—DHuS) Hub in 3–4 h. Hence, these products are suitable for a NRT service like that presented in this paper. AUTOWADE makes use of S1 Level-1 (L1) Ground Range Detected (GRD) products, whose spatial resolution is about $20 \times 20 \text{ m}^2$; S1 data are available in dual polarization (VV + VH) for the IWS mode. Considering both satellites of the S1 constellation, the repeat cycle of S1 is 6 days. Considering both ascending and descending orbits and the overlap of the orbits, the average revisit time is 2–3 days.

AUTOWADE has been conceived to work daily on the Italian territory, whose coverage is performed by means of 7 descending orbits (morning passes) and 6 ascending orbits (afternoon passes) as shown in Figure 1. For each orbit, the S1 GRD products are available as image slices for the purpose of data manageability. Each slice is a stand-alone product that can be processed independently. A total of 30 slices are included in the descending orbits covering Italy, while 34 slices are included in the ascending orbits.

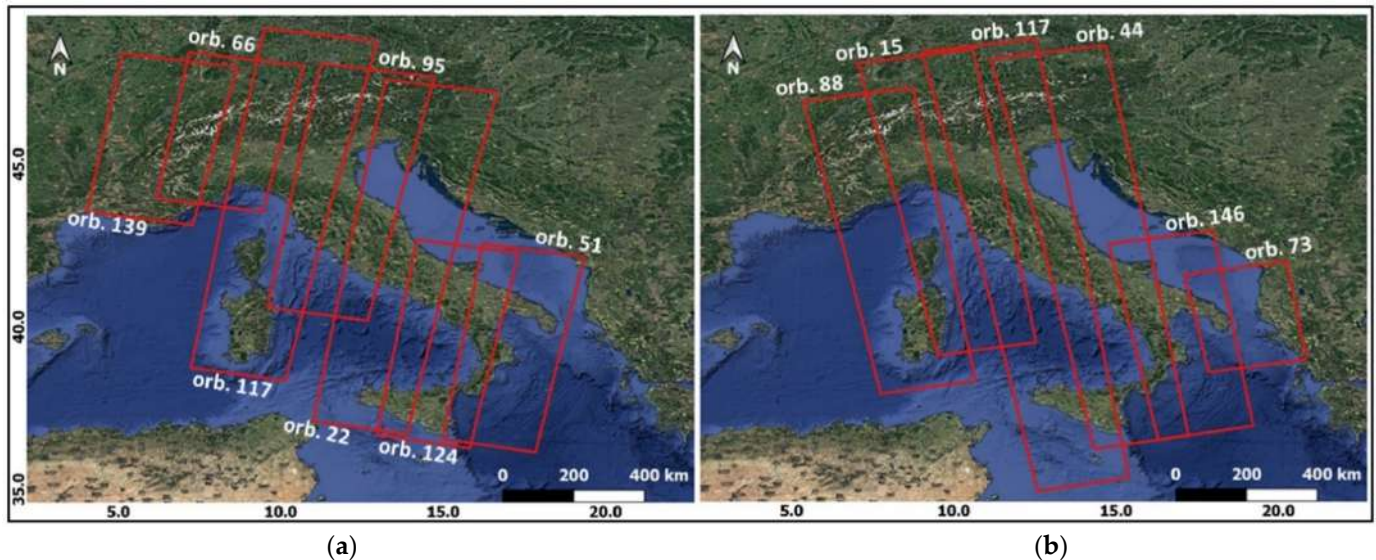


Figure 1. Portions of the Sentinel-1 orbits covering the Italian territory. Panel (a): descending orbits (morning overpasses); panel (b): ascending orbits (afternoon overpasses).

2.2. Ancillary Data

In order to perform the geocoding of the S1 GRD data, the 1-arcsecond (30 m) Shuttle Radar Topography Mission (SRTM) digital elevation model (DEM) is used by AUTOWADE. Recently, new DEMs have been proposed such as the corrected SRTM [32] and the Copernicus 30-m global DEM, referred to as GLO-30. The latter, open to the public since November 2020, will be tested in the following releases of AUTOWADE. A mosaicking of the SRTM tiles covering Italy has been performed once and for all during the design phase of the tool and, from this mosaic, a slope map has been extracted to be used in the generation of the exclusion mask (set of pixels where water mapping is unfeasible).

Another static layer is used by AUTOWADE in the generation of the exclusion mask, namely a land cover map produced by rasterizing the CORINE Land Cover (CLC) level 3 vector file at a spatial resolution of $20 \times 20 \text{ m}^2$ on the WGS84 reference ellipsoid (projection LATLON-WGS84). The most recent version (2018) of the CLC data, released in the frame of the Copernicus program and available through the catalog of the Copernicus Land Monitoring Service (Pan-European component), has been chosen. The land cover map also represents the master product used to generate the AUTOWADE-derived product and consists of $66,000 \times 58,500$ pixels.

AUTOWADE also uses a reference water mask. It is a static layer derived from the water and wetness (WAW) product available through the Copernicus Land Monitoring Service (Pan-European component—high-resolution layers). WAW is a thematic map that identifies permanent water, temporary water, permanent wetness, and temporary wetness. Only the pixels labelled as permanent water have been included in the reference water mask. For this class, the accuracy is expected to exceed 85% [33].

Not only static layers, but also constantly updated maps are included among the ancillary data. These maps are produced by another processor, described in [34], which works on Sentinel-2 (S2) level-2A (L2A) data. In particular, a map of Normalized Difference Vegetation Index (NDVI) and a map of snow cover, both projected on the CLC reference

grid, are used to search for flooded vegetation and to complement the exclusion mask. For each of the $66,000 \times 58,500$ pixels, these data are derived from the most recent S2 observation performed under cloud-free conditions. If the most recent S2 observation is older than one month, *NDVI* and snow cover data are not used, and flooded vegetation is not searched for. An example of *NDVI* map is shown in Figure 2, while a summary of the main characteristic of the ancillary layers is reported in Table 1. From Table 1, it can be noted that the spatial resolution of the CLC data is coarser than that of S1 and the other data. However, since AUTOWADE makes use of the CLC only to mask urban areas, the impact of the use of this relatively low-resolution data on the accuracy of the maps of floodwater/permanent water is expected to be quite small.

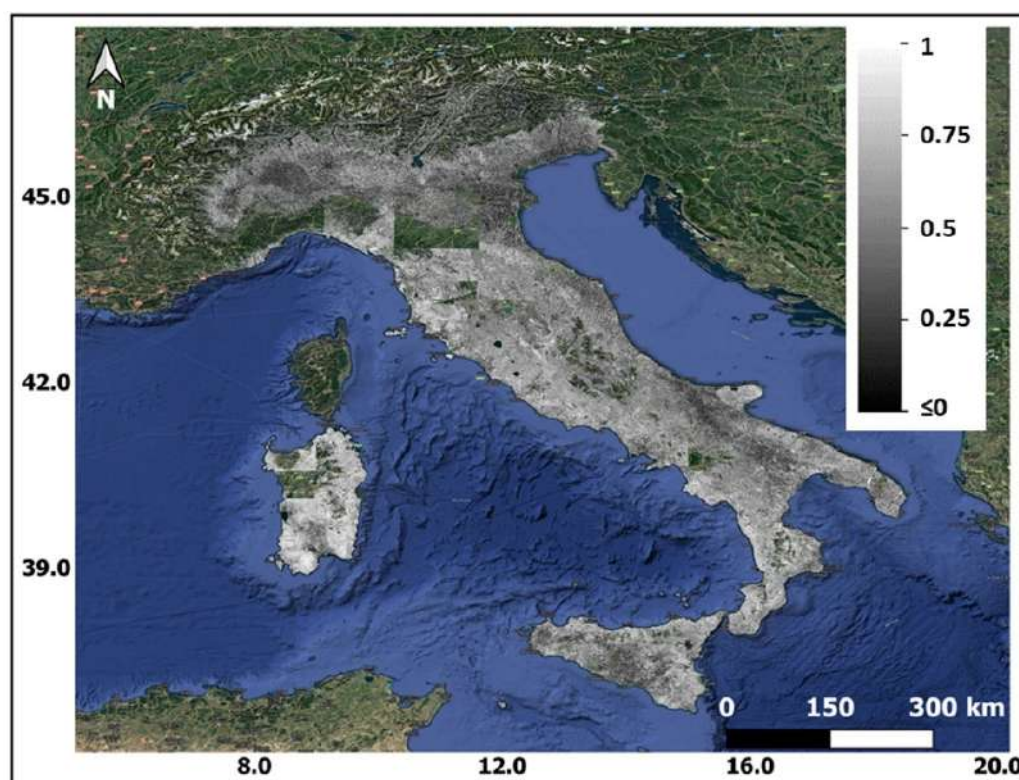


Figure 2. NDVI map updated on 12 January 2021. Gaps correspond to pixels where no cloud-free S2 data were available in the last 30 days (i.e., since 12 December 2020), or to pixels covered by snow, or water bodies.

Table 1. Spatial resolution and revisit frequency of the ancillary data.

	Spatial Resolution	Revisit Frequency
Static Layers		
Shuttle Radar Topography Mission (SRTM)	30 m	-
CORINE Land Cover (CLC)	100 m	-
Water and Wetness (WAW)	20 m	-
Dynamic Layers		
Normalized Difference Vegetation Index (<i>NDVI</i>) map from Sentinel 2	20 m	5 days
Snow cover map from Sentinel 2	20 m	5 days

2.3. Validation Data

CEMS-derived products have been mainly used to validate the open water mapping algorithm implemented in AUTOWADE. They have been generated in the framework

of the CEMS activations listed in Table 2. Usually, CEMS products are generated based on automatic extraction procedures, followed by an important/crucial step of validation based on visual interpretation by skilled operators. Within the CEMS portfolio, delineation products, which provide an assessment of the event's extent, have been selected. These products also include hydrography data useful to assess the AUTOWADE capability to map permanent water. For this latter purpose, hydrography data have been complemented by open water maps generated by applying the algorithm proposed in [35] to S2 images acquired under standard non-flooded conditions.

Table 2. Test cases considered in this study for open water mapping.

CEMS Activation Code	Time Period	Location	River Basin	Type of Flood	Area of Interest [ha]	Estimated Flooded Area [ha]
EMSR359	May 2019	Modena (Italy)	Secchia	Riverine flood	28,000	283
EMSR411	November 2019	Puget-sur-Argens (France)	Argens	Riverine flood	39,800	285
EMSR417	December 2019	Coimbra (Portugal)	Mondego	Riverine flood & dike breaches	147,600	9460
EMSR429	February 2020	Springfield Clonara (Ireland)	Shannon	Flash flood	7900	546
EMSR437	May 2020	Dax (France)	Adour	Riverine flood	40,668	1850
EMSR445	June 2020	Radauti-Prut (Romania)	Prut	Riverine flood	95,100	1358
EMSR492	January 2021	Mont De Marsan (France)	Adour	Flash flood	103,500	4899
EMSR496	January 2021	Rieti (Italy)	Turano	Riverine flood & dams emptying	8400	307
EMSR501	February 2021	Shkoder (Albania)	Buna	Riverine flood	100,500	5039
EMSR502	February 2021	Mallow (Ireland)	Blackwater	Riverine flood	22,500	470

The test cases in Table 2 have been selected based on the following constraints: (1) floods occurred in Europe, in order to take advantage of the Copernicus-derived ancillary data; (2) floods mapped by CEMS using S1 data; (3) floods for which a (at least partially) cloud free S2 image acquired close in time to the S1 one and under non-flooded conditions was available. In addition, events occurring in environments very different from the Italian one (like Scandinavia) have been neglected. Note that since the oldest Sentinel data are removed from the Copernicus Open Access Hub, only recent events (2019–2021) have been considered. The S1 slices used to generate the AUTOWADE-derived open floodwater/permanent water maps are listed in Table 3. It can be noted that, for each test case, even a pre-flood image has been used to generate the AUTOWADE-derived maps.

Table 3. S1-GRD slices used in this study for open water mapping.

CEMS Activation Code	Sentinel-1 Data	
EMSR359	S1B_IW_GRDH_1SDV_20190507T171356_20190507T171421_016141_01E5E8_5A61 S1A_IW_GRDH_1SDV_20190513T171426_20190513T171451_027212_031159_E494	pre-flood flood image
EMSR411	S1B_IW_GRDH_1SDV_20191119T053524_20191119T053549_018992_023D59_A320 S1A_IW_GRDH_1SDV_20191125T053615_20191125T053640_030063_036EEE_FF7D	pre-flood flood image
EMSR417	S1A_IW_GRDH_1SDV_20191211T064251_20191211T064316_030297_03770D_7B8C S1A_IW_GRDH_1SDV_20191223T064251_20191223T064316_030472_037D16_1012	pre-flood flood image
EMSR429	S1A_IW_GRDH_1SDV_20200217T182251_20200217T182316_031296_0399B6_DA09 S1B_IW_GRDH_1SDV_20200223T182202_20200223T182227_020400_026A63_888F	pre-flood flood image
EMSR437	S1A_IW_GRDH_1SDV_20200507T060905_20200507T060930_032455_03C224_66CF S1B_IW_GRDH_1SDV_20200513T060818_20200513T060843_021559_028EE8_45FA	pre-flood flood image
EMSR445	S1A_IW_GRDH_1SDV_20200620T160959_20200620T161024_033103_03D5BD_2501 S1B_IW_GRDH_1SDV_20200626T160915_20200626T160940_022207_02A256_2724	pre-flood flood image
EMSR492	S1A_IW_GRDH_1SDV_20201221T060912_20201221T060937_035780_04301A_3C7A S1A_IW_GRDH_1SDV_20210102T060911_20210102T060936_035955_04362E_97BF	pre-flood flood image

Table 3. Cont.

CEMS Activation Code	Sentinel-1 Data	
EMSR496	S1A_IW_GRDH_1SDV_20210115T051146_20210115T051211_036144_043CD9_7753 S1A_IW_GRDH_1SDV_20210127T051146_20210127T051211_036319_0442F1_EF15	pre-flood flood image
EMSR501	S1B_IW_GRDH_1SDV_20201214T163224_20201214T163249_024701_02F011_8A13 S1B_IW_GRDH_1SDV_20210212T163221_20210212T163246_025576_030C3D_87F3	pre-flood flood image
EMSR502	S1B_IW_GRDH_1SDV_20210217T182208_20210217T182233_025650_030EBA_FB05 S1A_IW_GRDH_1SDV_20210223T182257_20210223T182322_036721_0450DC_EC43	pre-flood flood image

Generally, CEMS-derived products do not include flooded vegetation if they are produced using SAR data. To verify the AUTOWADE capability to detect flooded vegetation adjacent to open water, two events recently that occurred in Italy have been considered as test cases (Table 4). For the first event that occurred in October 2020 in the Vercelli district, an S2 image acquired on the same day as the S1 flood image has been used as reference data. For the flood that occurred in January 2021 (also mapped by CEMS: EMSR496 in Table 2), aerial photos were available as reference. From Table 4, it can be noted that pre-flood S2 data have been utilized to estimate *NDVI* under non-flooded conditions (Section 2.2).

Table 4. S1-GRD slices and S2-L2A tiles used in this study for flooded vegetation mapping.

Instrument	Data		Location
Sentinel-1	S1B_IW_GRDH_1SDV_20200927T172230_20200927T172255_023564_02CC5D_1886 S1A_IW_GRDH_1SDV_20201003T172311_20201003T172336_034635_040884_7989	pre-flood flood image	Vercelli (Italy)
Sentinel-2	S2A_MSIL2A_20200928T102031_N0214_R065_T32TMR_20200928T131819 S2B_MSIL2A_20201003T101759_N0214_R065_T32TMR_20201003T145325	pre-flood flood image	
Sentinel-1	S1A_IW_GRDH_1SDV_20210115T051146_20210115T051211_036144_043CD9_7753 S1A_IW_GRDH_1SDV_20210127T051146_20210127T051211_036319_0442F1_EF15	pre-flood flood image	Rieti (Italy)
Sentinel-2	S2A_MSIL2A_20201221T100431_N0214_R122_T33TUH_20201221T115632	pre-flood	

3. Methods

In the following, the main functionalities of AUTOWADE, schematically shown in Figure 3, are described in detail.

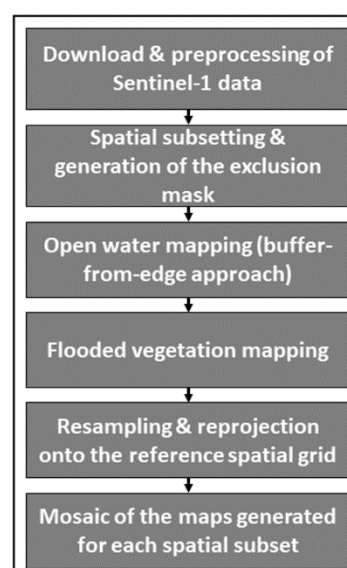


Figure 3. Block diagram of the AUTOWADE's main functionalities.

3.1. Download and Preprocessing of Sentinel-1 Data

The first block of the AUTOWADE tool performs the operations of searching, downloading, and unzipping S1 L1 GRD data by using a script in Python language, as shown in the left side of Figure 4. It takes advantage of the freely available Sentinelsat tool (<https://pypi.org/project/sentinelsat/>, accessed on 31 March 2021) that enables users to automatically search and download Sentinel-1/2/3/5p data. For the script, the following Sentinelsat inputs are used: (1) URL of the Copernicus Open Access Hub; (2) start date; (3) product type (GRD in this case); (4) Search polygon in GeoJSON format (corresponding to Italy in this case).

The downloading script is scheduled to run every hour (365 days-a-year) to continuously verify the availability of new S1 images; in this way, possible delays in the production and delivery of L1 GRD products are managed.

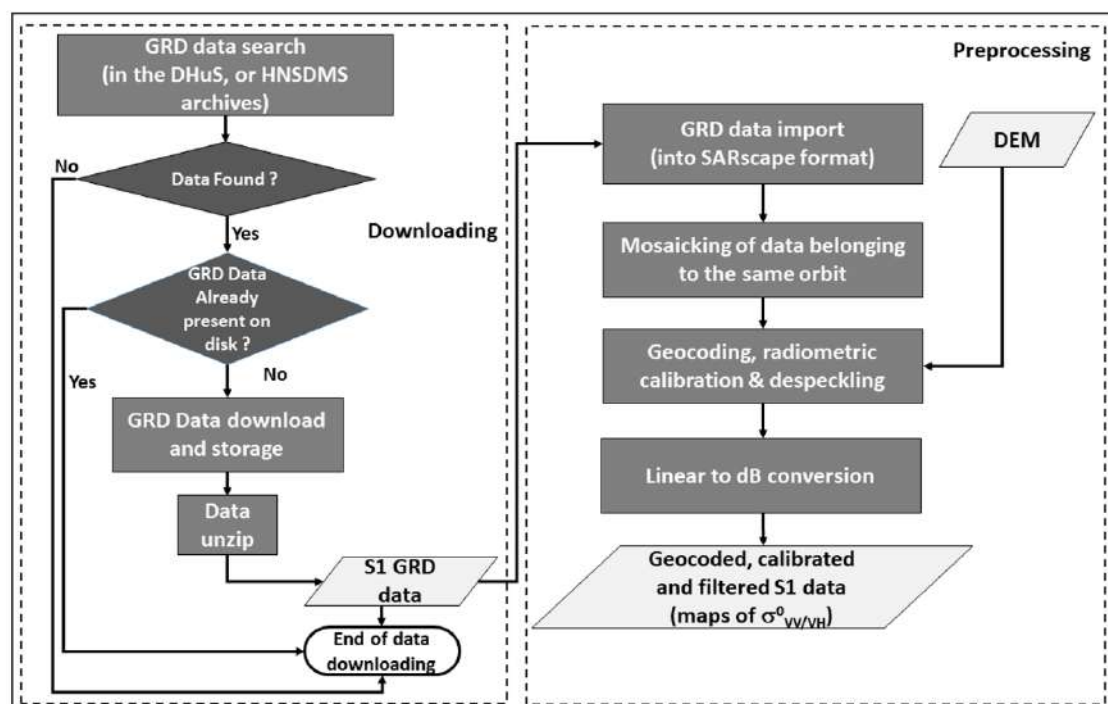


Figure 4. Block diagram of the script for S1 data downloading and preprocessing implemented in AUTOWADE.

The preprocessing of S1 data is schematized in the right side of Figure 4; it is performed using the SARscape COTS software, available as a tool of the IDL/ENVI commercial software package. In particular, a SARscape batch script in IDL language has been created; it is scheduled to be executed twice a day (at 02:00 AM for the afternoon passes of the previous day and 06:00 PM for morning passes) 365 days-a-year, provided that new GRD products are available. The S1 data are initially imported into SARscape and the slices belonging to the same orbit are mosaicked. Then, the data are radiometrically calibrated (backscattering coefficient σ^0) according to the radar equation. The calibration involves correction for the scattering area (each output pixel is normalized for the real illuminated area of each resolution cell), the antenna gains pattern, and the sensor-to-ground distance variation from near range to far range. Moreover, a correction factor based on a modified cosine model [36] is applied to the backscattering coefficient to compensate for range variations.

Calibrated data are geocoded using the SRTM DEM introduced in Section 2.2; a pixel size of $15 \times 15 \text{ m}^2$ has been chosen for the geocoded data. To reduce the speckle noise characteristic of any SAR image, the Enhanced Lee Filter [37] with a window size of 5×5 pixels is applied. Finally, the backscattering data are converted in dB units. An example of the output of the preprocessing phase is shown in Figure 5.

In order to distinguish between floodwater and permanent water, AUTOWADE adopts a change detection approach (Section 3.2.2) that analyzes pairs of S1 images acquired from the same orbit; to this aim, the preprocessing step creates a data archive where calibrated, geocoded, and filtered data acquired from different orbits are distinguished.

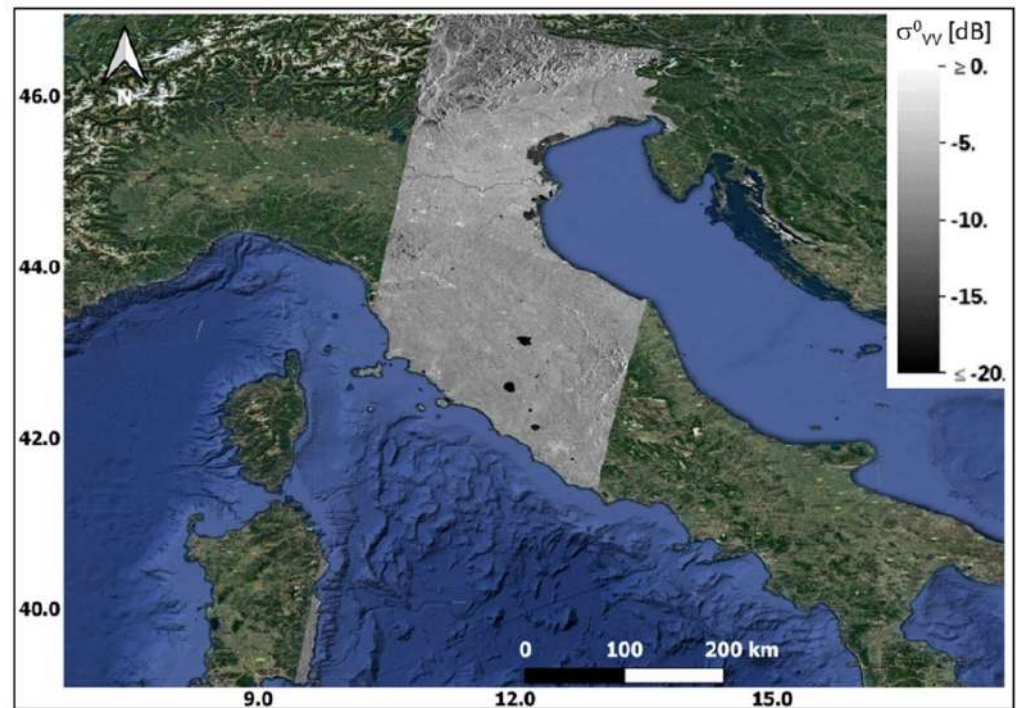


Figure 5. Example of output of the S1 data preprocessing block of AUTOWADE (relative orbit 95 and VV polarization).

3.2. The Floodwater/Permanent Water Mapping Algorithm

The execution of the floodwater/permanent water mapping algorithm follows immediately the execution of the preprocessing batch script described above; thus, the algorithm runs twice a day. It has been written in IDL language and takes advantage of the possibility to launch ENVI routines through specific IDL instructions. The algorithm is divided in four blocks; they are described hereafter.

3.2.1. Preliminary Operations

The preliminary operations carried out by the water mapping algorithm are shown in Figure 6, where t_2 indicates current time, while t_1 indicates the time of the previous S1 acquisition from the same orbit (typically $t_2 - t_1 = 6$ days). The spatial subsetting divides the S1 mosaicked data in frames (i.e., smaller rasters having a maximum number of lines equal to 17,000) in order to avoid dealing with big rasters, which may require an excessive use of memory. The operations described hereafter are referred to a single frame and are sequentially performed until all the frames are processed.

The ancillary data and the map produced using the data acquired at t_1 are resampled and reprojected onto the spatial grid of the current frame. Then, the exclusion mask is derived from the ancillary data to exclude from the classification areas where radar backscatter is insensitive to the presence of surface water, such as urban areas (identified through the CLC data), dense vegetation (pixels where $NDVI$ is larger than a threshold equal to 0.7), and areas with complex topography (pixels having a slope larger than 7°). The last preliminary operation is the application of a difference operator (corresponding to the log-ratio operator because the data are in dB units), which allows AUTOWADE to compare pixel by pixel the S1 images acquired at t_1 and at t_2 on the geographical area corresponding to the current frame.

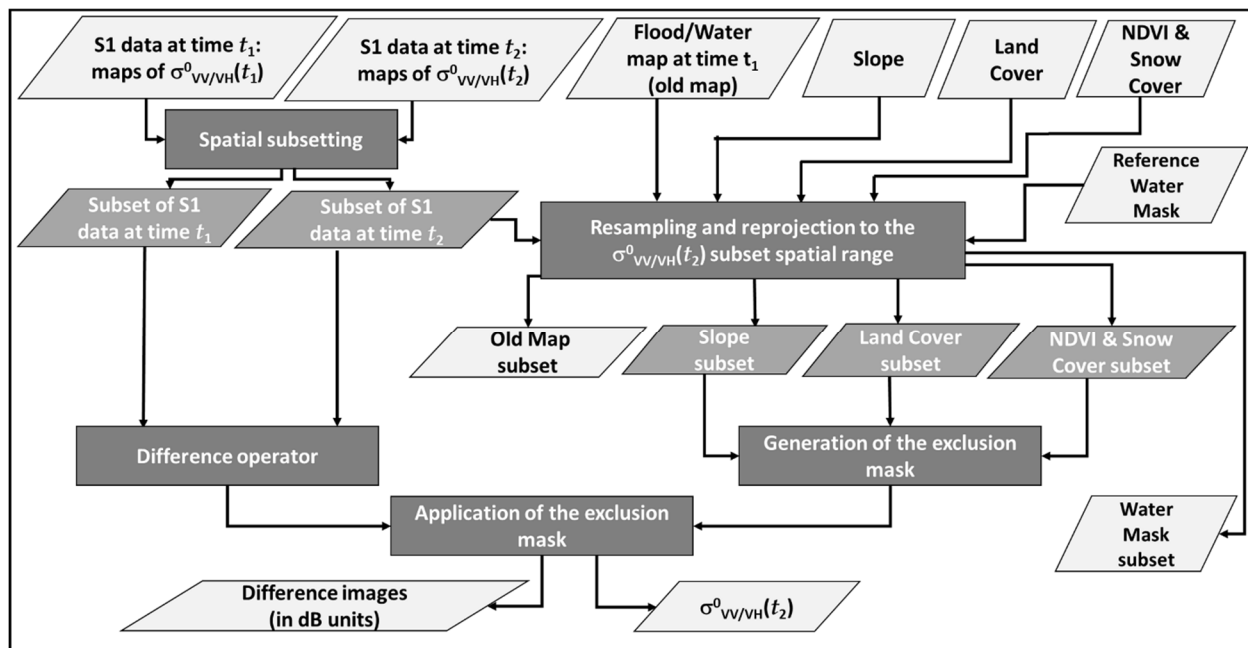


Figure 6. Flowchart of the preliminary operations performed by AUTOWADE. Dark gray rectangles represent operations; parallelograms represent data (light gray: input/output data, dark gray: intermediate data).

3.2.2. The Buffer-from-Edge (BFE) Approach to Map Open Water

The core of the AUTOWADE tool is represented by the algorithm designed to map open floodwater and permanent water; its flowchart is shown in Figure 7. The algorithm is organized in two phases. In the first phase, open water is detected by processing the S1 data at time t_2 (left side of Figure 7). In the second phase, the same operations performed on $\sigma_{VV}^0(t_2)$ are applied to the image difference to distinguish open floodwater from permanent water (right side of Figure 7). Only co-polarized data are used here, while VH data are successively used to identify flooded vegetation (Section 3.2.4).

The algorithm is based on the BFE approach, which has been derived from the buffer-from-cluster approach proposed in [35] for optical data. The BFE approach takes advantage of the availability of the reference water mask derived from the WAW product and combines different image processing techniques, such as the Iterative Self-Organizing Data Analysis Technique Algorithm (ISODATA) [38], the Roberts edge filter [39], the Otsu's thresholding [40], and the region growing (RG) [41,42].

The first step of the BFE approach consists of the application of the ISODATA, which is an unsupervised clustering algorithm that separates groups of objects in a scene (more details on the ISODATA can be found in Appendix A). The optimum number of clusters is not known, so it is generally chosen to be conservatively high [38]. Hence, although in this case the goal is to distinguish water from non-water, a maximum number of 10 clusters has been chosen. Since backscattering from open water is very low (see the Introduction), the objects belonging to the cluster presenting the lowest median of the values of $\sigma_{VV}^0(t_2)$ are selected and labelled as the clustering-derived water area (CDWA). Median value is used instead of mean value being less sensitive to outliers. Then, a reliable threshold separating water pixels from non-water ones is determined.

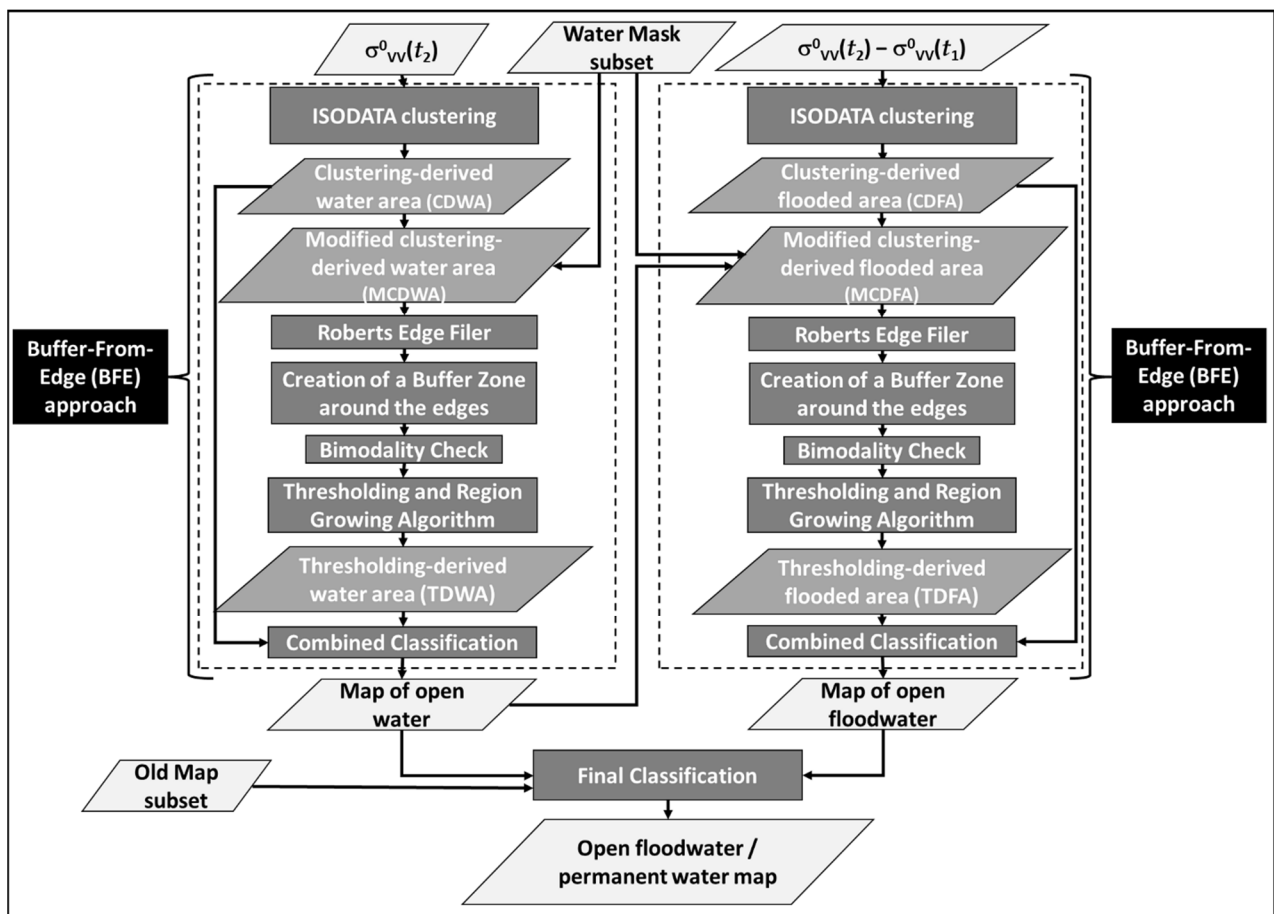


Figure 7. Flowchart of the open water mapping algorithm implemented in AUTOWADE. Dark gray rectangles represent operations; parallelograms represent data (light gray: input/output data, dark gray: intermediate data).

A fully automated algorithm requires to compute the threshold in an automatic way by using methods such as that proposed by Otsu [40]. However, automatic thresholding works well only if the fraction of water pixels is large enough to give rise to a detectable mode (i.e., the population composed of water and non-water pixels exhibits a bimodal distribution). To identify a subset of a S1 image whose histogram is characterized by two distinguishable modes, the CDWA is firstly combined with the reference water mask to include only the objects that contain permanent water bodies. In this way, the modified clustering-derived water area (MCDWA), which contains only open water detected by S1, is created. Then, a Roberts edge filter [39] is applied to the MCDWA to identify the water-land edge. Note that the Roberts filter is not directly applied to the reference mask because it may not represent the current water-land edge (for instance in case of river overflow). Successively, two buffer zones, whose buffering distance may be iteratively enlarged, are created around the edge. One buffer zone is included in the MCDWA (and is likely composed by water pixels); the other one is included neither in the MCDWA, nor in the CDWA (and is likely composed by non-water pixels).

An example illustrating the location of the edge identified by the Roberts filter and the buffer zones is shown in Figure 8c. Looking at Figure 8, it can be noted that the pixels appearing red in panel (a), likely flooded because $\sigma_{VV}^0(t_2)$ is much smaller than $\sigma_{VV}^0(t_1)$, are not comprised in the cyan buffer zone in panel (c) because of the intersection between the original CDWA and the reference water mask, performed to be sure that the cyan buffer zone contains only water pixels.

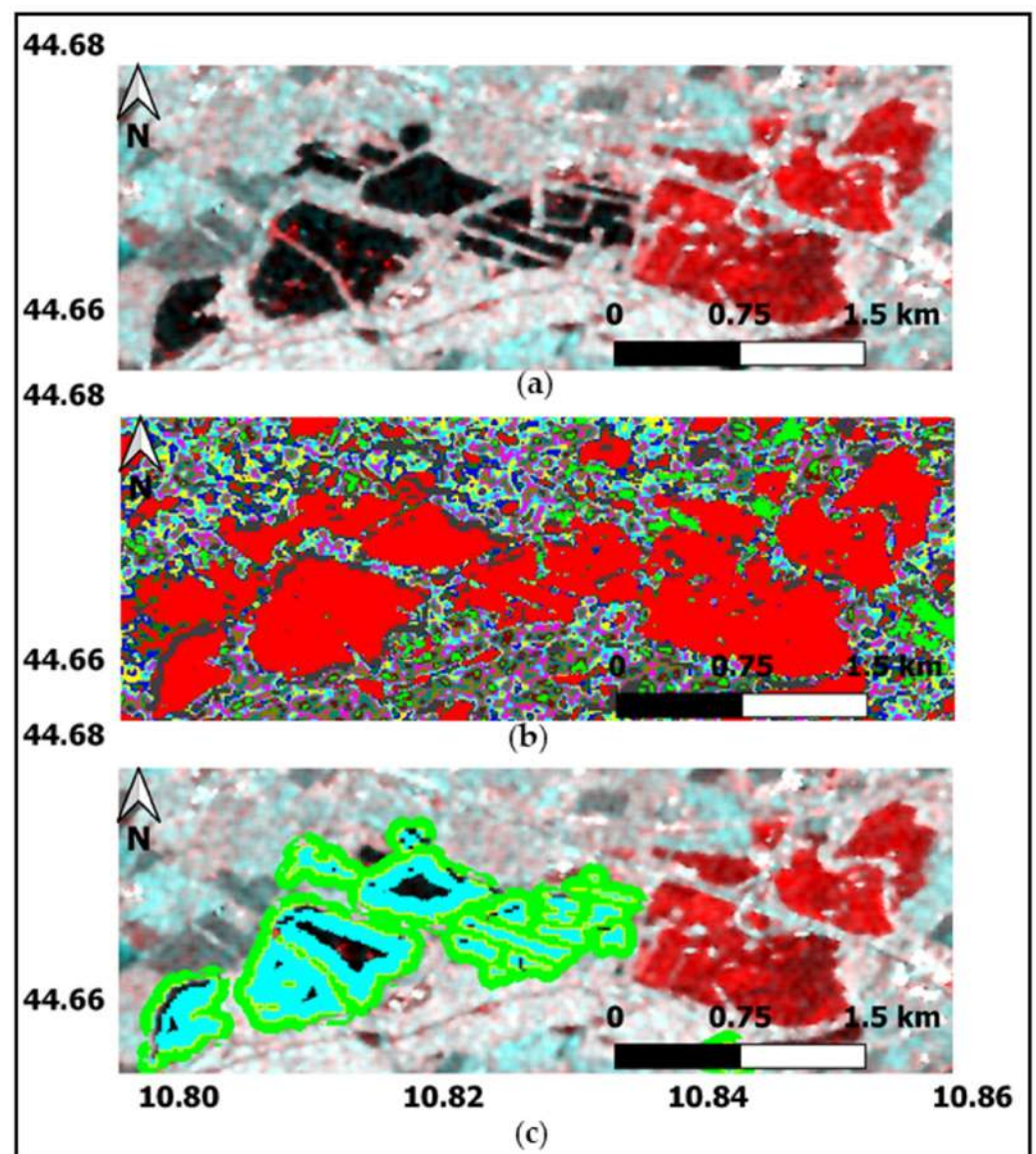


Figure 8. Panel (a): RGB false color images created using the S1 data gathered to produce the floodwater/permanent water map for the EMSR359 case study and zooming on the area affected by the flood; red: pre-flood image (at t_1), green/blue: flood image (at t_2). Panel (b): output of the ISODATA applied to the flood image (CDWA in red). Panel (c): same as panel (a), but with superimposed the land-permanent water edge (yellow), the buffer zone included in the MCDWA (cyan) and the buffer zone included neither in the MCDWA, nor in the CDWA (green).

The creation of the two buffer zones (cyan and green in Figure 8c) aims at selecting a set of pixels containing a comparable amount of water and non-water pixels. To verify the bimodality of the histogram of the backscatter values of this set of pixels, a Gaussian mixture model (GMM) is assumed. The population formed by the pixels included in the buffer zones is therefore considered as represented by two normally distributed subpopulations (water and non-water pixels). The rationale is that, with an increasing equivalent number of looks, the PDF of the log-transformed σ^0 can be modeled as a Gaussian distribution [24]. Then, a non-linear least square fit to a Gaussian function is computed for the histograms of the two buffer zones. Figure 9 shows, for the same case study considered in Figure 8, the histograms of the pixel values of the two buffer zones, and the Gaussian functions fitting the histograms.

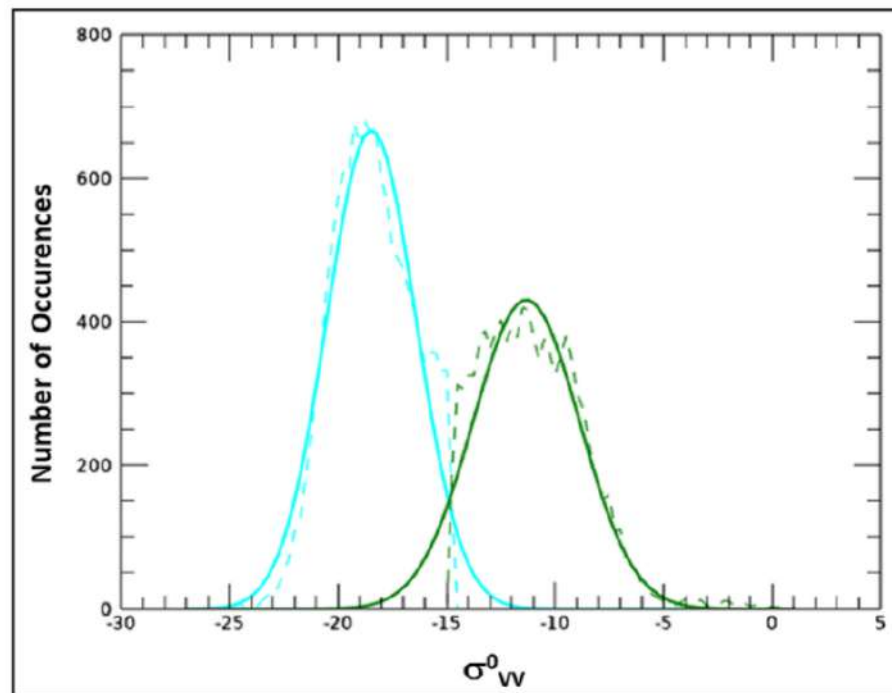


Figure 9. Histogram of the σ^0 values of the subpopulations composed of the pixels belonging to the buffer zone included in the MCDWA (cyan dashed lines) and the buffer zone included neither in the MCDWA, nor in the CDWA (green dashed lines). Solid lines represent the Gaussian functions fitting the histograms. The EMSR359 case study is considered.

The bimodality of the overall histogram is tested by evaluating the Ashman's D coefficient [43], the bimodality coefficient [44,45], and the ratio between the modes. If these quantities are larger than threshold values determined in previous literature (see Appendix B for details), the bimodality test is considered as passed. Otherwise, the buffer zone containing the smallest number of pixels is enlarged and the bimodality test is repeated. This iterative process stops when the bimodality test is passed or a maximum number of 100 repetitions is reached.

If the bimodality check is passed, the Otsu's automatic method [40] is used to compute a threshold value (Th_{Otsu_w}). Then, RG is applied, as done in [18,26,46], in order to account for the spatial context that is not considered if changed pixels are simply identified based on a threshold value, without any tolerance. RG analyses neighboring pixels of a set of seed points and determines whether the pixel neighbors should be added to the seed region based on a tolerance criterion [41,42]. The following relationships are used to determine the seed region and the tolerance:

$$i \in \text{seed region} \implies \sigma_{VV}^0(i) < \sigma_{VV_seed}^0 = 0.5 \cdot (Th_{Otsu_w} + \mu_w) \quad (1)$$

$$\sigma_{VV_Tolerance}^0 = (\mu_w + 2s_w) \quad (2)$$

where i is a pixel of the processed frame, μ_w and s_w are the mean value and standard deviation of the Gaussian distribution fitting the histogram of the σ_{VV}^0 values of the pixels in the buffer zone included in the MCDWA (cyan solid line in Figure 9). From Equation (1), it can be deduced that the seed region is formed by the pixels whose backscattering is less than the mean value between the mode of the aforementioned Gaussian distribution (corresponding to the mean) and Th_{Otsu_w} .

If the bimodality test is not passed after 100 repetitions of the iterative process described above, default values derived from the analysis of the test cases reported in Table 2 are used to identify the seed region and the tolerance, namely $\sigma_{VV_seed}^0 = -17$ dB and $\sigma_{VV_Tolerance}^0 = -14$ dB.

The set of pixels selected through Equations (1) and (2) is denoted as the thresholding-derived water area (TDWA). The BFE approach combines the original CDWA and the TDWA to obtain the map of open water based on the following scheme:

- pixels belonging to both the CDWA and the TDWA are classified as open water;
- pixels belonging only to the TDWA are classified as open water if they are located in a buffer zone of buffering distance 1 km created around the water area determined according to the previous point.

3.2.3. Discrimination between Open Floodwater and Permanent Water

To identify floodwater, the BFE approach is applied to the difference image, i.e., to the map of $\Delta\sigma_{VV}^0 = \sigma_{VV}^0(t_2) - \sigma_{VV}^0(t_1)$, as schematized in the right panel of Figure 7. In this case, the objects belonging to the cluster presenting the lowest median of the values of $\Delta\sigma_{VV}^0$ are selected and labelled as the clustering-derived flooded area (CDFA). The latter is then modified to include only the objects that contain open water according to the classification applied to $\sigma_{VV}^0(t_2)$, but do not contain permanent water bodies according to the reference water mask. In this way the modified clustering-derived flooded area (MC DFA) likely contains only flooded pixels, i.e., pixels whose backscattering coefficient significantly decreased with respect to that measured at time t_1 . The Roberts filter is then applied to detect the floodwater-land edge and two buffer zones are created around the edge to select a set of pixels exhibiting a bimodal histogram of the $\Delta\sigma_{VV}^0$ values. For the same example considered in Figure 8, Figure 10 shows the floodwater-land edge and the buffer zones created around it.

A GMM has been assumed for the distribution of flooded and non-flooded pixels in the difference image (even the distribution of the log-ratio SAR image is expected to follow the Gaussian model [24]). For the population of pixels included in the two buffer zones, the bimodality test is performed in a similar way to that described in the previous paragraph. If the bimodality check is passed, a threshold value (Th_{Otsu_f}) is computed through the Otsu's method. Then, the following relationships are used to derive the seed region and the tolerance:

$$i \in \text{seed region} \implies \Delta\sigma_{VV}^0(i) < \Delta\sigma_{VV_seed}^0 = 0.5 \cdot (Th_{Otsu_f} + \mu_f) \quad (3)$$

$$\Delta\sigma_{VV_Tolerance}^0 = (\mu_f + 2s_f) \quad (4)$$

where μ_f and s_f are the mean value and standard deviation of the Gaussian distribution fitting the histogram of the $\Delta\sigma_{VV}^0$ values of the pixels in the buffer zone included in the MC DFA. Through Equations (3) and (4), the thresholding-derived flooded area (TDFA) is identified.

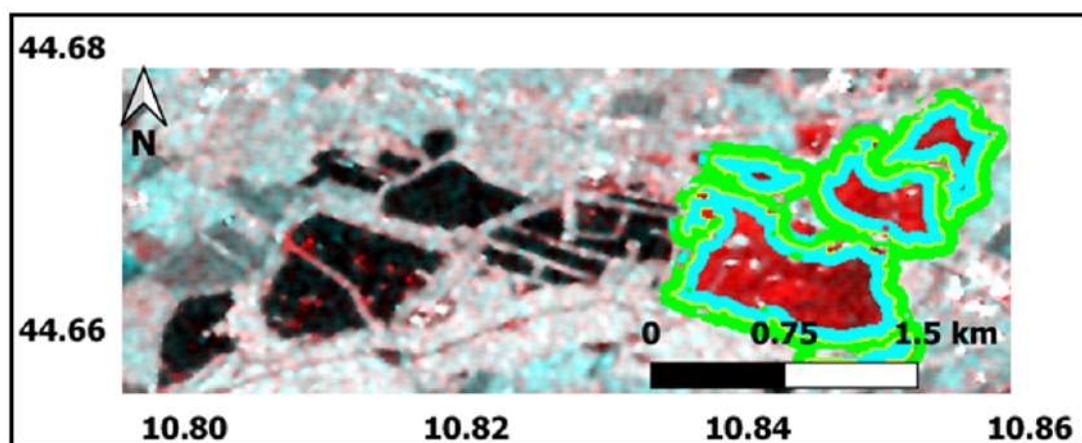


Figure 10. Same as Figure 8c, but with superimposed the land-floodwater edge (yellow), the buffer zone included in the MC DFA (cyan) and the buffer zone included neither in the MC DFA, nor in the CDFA (green).

The original CDFA and the TDFA are combined to obtain the map of flooded pixels based on the following scheme:

- pixels belonging to both the CDFA and the TDFA are assigned to the class of flooded pixels;
- pixels belonging only to the TDFA are assigned to the class of flooded pixels if they are located in a buffer zone of buffering distance 1 km created around the flooded area determined according to previous point.

The outputs of the two BFE procedures are finally combined to perform the discrimination between open floodwater and permanent water (final classification box in Figure 7). The following scheme is used by AUTOWADE:

- pixels belonging to class of open water are finally classified as open floodwater if they also belong to the class of flooded pixels, or if they have been classified as open floodwater at time t_1 (old map, see Figure 7);
- pixels belonging to class of open water are finally classified as permanent water if they also belong to the reference water mask, or if they are adjacent to the reference water mask and do not belong to the class of flooded pixels, or if they have been classified as permanent water at time t_1 (old map at the bottom of Figure 7).

All the flooded pixels grouped in patches smaller than 20,000 m² (50 pixels) are filtered out, thus assuming 20,000 m² as minimum mapping unit. Obviously, pixels comprised in the exclusion mask cannot be classified as open floodwater or permanent water.

3.2.4. Flooded Vegetation

The key to detect flooded vegetation using backscattering data is the double bounce backscattering. It occurs when the portion of the radar energy that is specularly reflected by the ground hits the plant stalks that act like dihedral corner reflectors and return the incoming energy back to the radar sensor [7]. If calm water covers the ground, most of the incoming radar energy is specularly reflected and the intensity of the double-bounce effect increases; this may imply a significant increase of the backscatter with respect to that measured under non-flooded conditions, i.e., large values of $\Delta\sigma_{VV}^0$.

However, flooded vegetation does not generally have a clear and unique radar signature that can be easily detected. First of all, the double bounce is the prevailing effect of flooded vegetation if the penetration into the canopy is sufficient [8]. In dense vegetation, volume scattering hampers the detection of floodwater. This is the reason why pixels with $NDVI > 0.7$ are comprised in the exclusion mask. Moreover, even an increase of soil moisture and/or soil roughness (caused for instance by ploughing activities) produces large values of $\Delta\sigma_{VV}^0$. Hence, simply searching for increases of the backscatter may cause commission errors. Recently, the use of cross-polarized data has been suggested to better detect the double bounce [11,47,48] considering that, in principle, the double bounce does not give rise to depolarization, so that small values of $\Delta\sigma_{VH}^0 = \sigma_{VH}^0(t_2) - \sigma_{VH}^0(t_1)$ are expected in flooded vegetation.

The procedure adopted to identify flooded vegetation in AUTOWADE is shown in Figure 11. The output of the ISODATA applied to $\Delta\sigma_{VV}^0$ is analyzed and the objects belonging to the cluster presenting the highest median of the values of $\Delta\sigma_{VV}^0$ are selected. Then, to reduce the risk of making commission errors, only objects adjacent to areas classified as flooded are maintained, also considering that, as discussed in the Introduction, the objective is to fill the gaps typically present in flood maps. In practice, an object is maintained if it is connected to a buffer zone of two pixels arounds floodwater, created to account for imprecisions in the identification of the objects in the scene (e.g., due to residual spackle). Successively, the mean values of $NDVI$ (denoted as \overline{NDVI}), $\Delta\sigma_{VV}^0$ ($\overline{\Delta\sigma_{VV}^0}$) and $\Delta\sigma_{VH}^0$ ($\overline{\Delta\sigma_{VH}^0}$) are computed for each selected object. Objects having $\overline{NDVI} \leq 0.2$ are removed since in this case the backscatter increase is ascribed to an increase of soil moisture and/or roughness. Remaining objects are assigned to the class of flooded vegetation according to a fuzzy logic-based approach. Through a standard S fuzzy membership

function (see Appendix C for more details about fuzzy logic), a degree of membership to the class of flooded vegetation is assigned, depending on the values of $\overline{\Delta\sigma_{VV}^0}$, $\overline{\Delta\sigma_{VH}^0}$, and the percentage (p) of the object's edge pixels connected to open water in the following way:

$$d_1 = S\left(x = \overline{\Delta\sigma_{VV}^0}, x_1 = 0 \text{ dB}, x_2 = 4 \text{ dB}\right) \quad (5)$$

$$d_2 = S\left(x = \overline{\Delta\sigma_{VV}^0} - \overline{\Delta\sigma_{VH}^0}, x_1 = 0 \text{ dB}, x_2 = 6 \text{ dB}\right) \quad (6)$$

$$d_3 = S\left(x = p, x_1 = 0\%, x_2 = 100\%\right) \quad (7)$$

where d_1 , d_2 , and d_3 are degrees of membership, x is the independent variable, x_1 and x_2 are the parameters of the S function (see Figure 11). Through Equations (5)–(7), maximum membership (equal to 1) to the class of flooded vegetation is given to objects having $\overline{\Delta\sigma_{VV}^0} > 4 \text{ dB}$, $\overline{\Delta\sigma_{VV}^0} - \overline{\Delta\sigma_{VH}^0} > 6 \text{ dB}$ and totally surrounded by open water. The combination of the membership's degrees is carried out by computing their average and if the average is larger than 0.5, an object is labelled as flooded vegetation (defuzzification box in Figure 11).

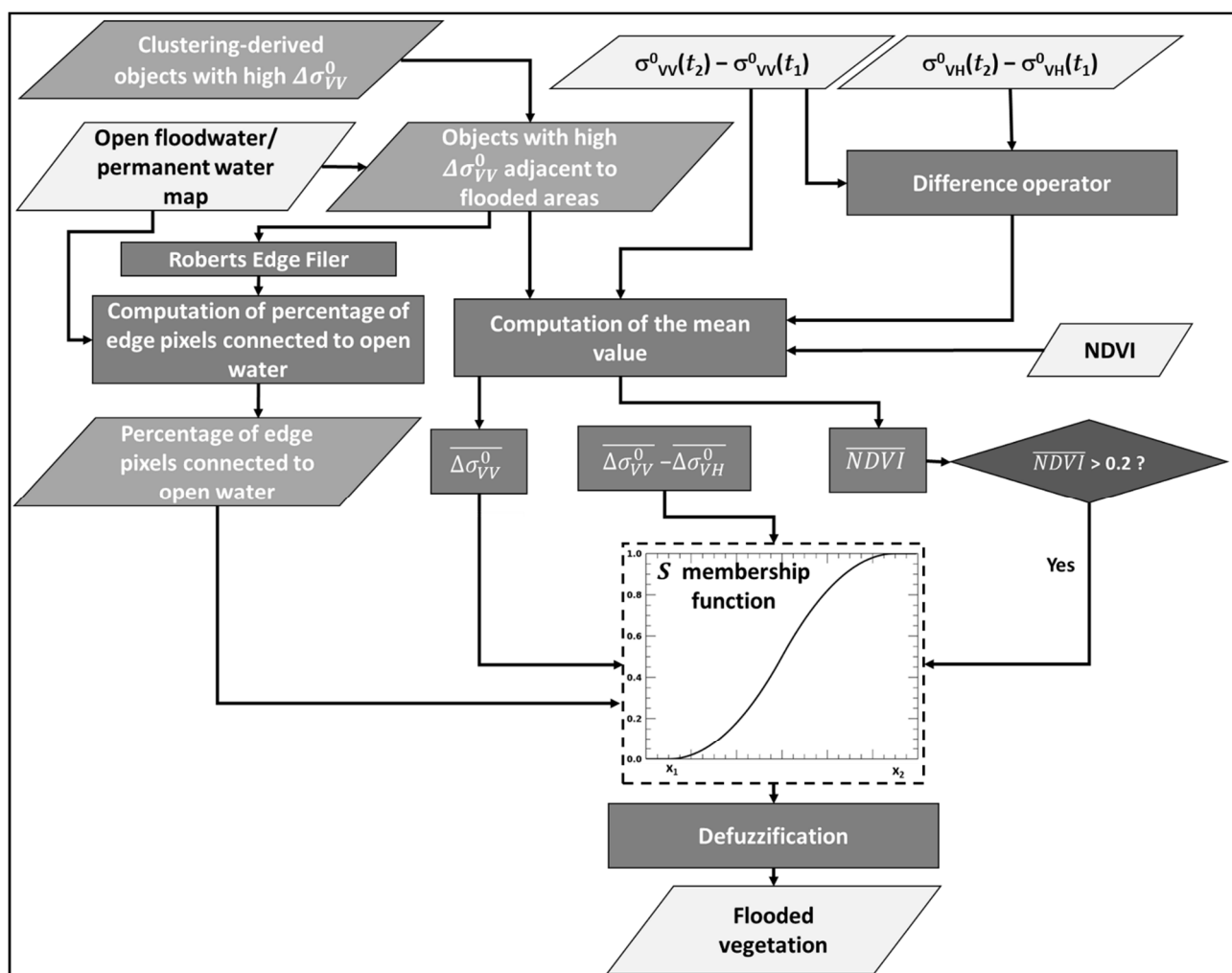


Figure 11. Flowchart of the algorithm developed to map flooded vegetation implemented in AUTOWADE. Dark gray rectangles represent operations; parallelograms represent data (light gray: input/output data, dark gray: intermediate data).

3.3. Validation

To quantitatively represent the results of the comparison between CEMS-derived maps and AUTOWADE-derived open floodwater/permanent water maps, a confusion matrix

has been computed for each case study listed in Table 2, assuming the CEMS-derived maps as reference data. A confusion matrix summarizes the performance of a classification algorithm; three thematic classes have been considered: (1) non-water, (2) open floodwater, (3) permanent water. From the confusion matrices, the following accuracy metrics have been derived: overall accuracy (OA), kappa coefficient (κ), F1-score (computed as the arithmetic mean of the per-class F1-scores [49]), errors of commission (ϵ_{comm}) and omission (ϵ_{om}) for the classes of open floodwater and permanent water.

It must be considered that the classes of water pixels are often underrepresented compared to the non-water class. This implies that very high values of OA can be easily obtained. To tackle this problem at least partially, limited geographic areas have been considered to derive the confusion matrices. The boundaries of the geographic areas have been determined using the “area of interest” shapefile included in the CEMS data (see [34] for more details), whose size is reported in Table 2 (6th column).

To further evaluate the quality of the AUTOWADE-derived maps, for each test case, the total extent (in ha) of the area classified as open floodwater has been calculated to be compared with the total flooded surface estimated by CEMS (Table 2, last column). The percentage of the flooded surface with respect to the size of the area of interest (AOI) has been computed too.

4. Results

4.1. Results of the BFE Approach Implemented in AUTOWADE

The intermediate results of the various steps of the BFE approach and the final map are shown in Figure 12 for the Modena test site (EMSR359, Table 2). It can be noted that the output map (panel d) is basically derived from the maps of TDWA (panel e) and TDFA (panel f). The maps of CDWA and CDFA, derived from the ISODATA, correspond to the red pixels in panels b,c. As expected, the maps of CDWA and CDFA are very noisy. Hence the need to combine the CDWA with the reference water mask to select the objects actually corresponding to water bodies (MCDWA). Similarly, the CDFA is modified to select the objects that contain open water, but do not contain permanent water bodies (MCDFA).

4.2. Results of the Flooded Vegetation Mapping Method Implemented in AUTOWADE

A full example of the results of the flooded vegetation algorithm for the Vercelli test case (Table 4) is shown in Figure 13. Many objects belong to the cluster of high $\Delta\sigma_{VV}^0$, most of them because of the increase of soil moisture due to rain; hence the need to focus on objects adjacent to open water having $\overline{NDVI} > 0.2$ to limit confusion between backscatter increases due to soil moisture variations and the presence of a double bounce structure formed by the horizontal water surface and vertical stems. The AUTOWADE-derived floodwater map (panel e) underestimates floodwater mapped using S2 (red line in panel a). This is partially due to the water receding, considering that S2 data were acquired in the morning of 3 October 2020, i.e., few hours after the peak of the Vercelli event; conversely, S1 data were acquired in the afternoon (about 7 h later than S2 data). Nevertheless, including flooded vegetation in the AUTOWADE-derived classification, the omission error reduces from 45% to about 40%, with a negligible increase of the commission error (around 5%).

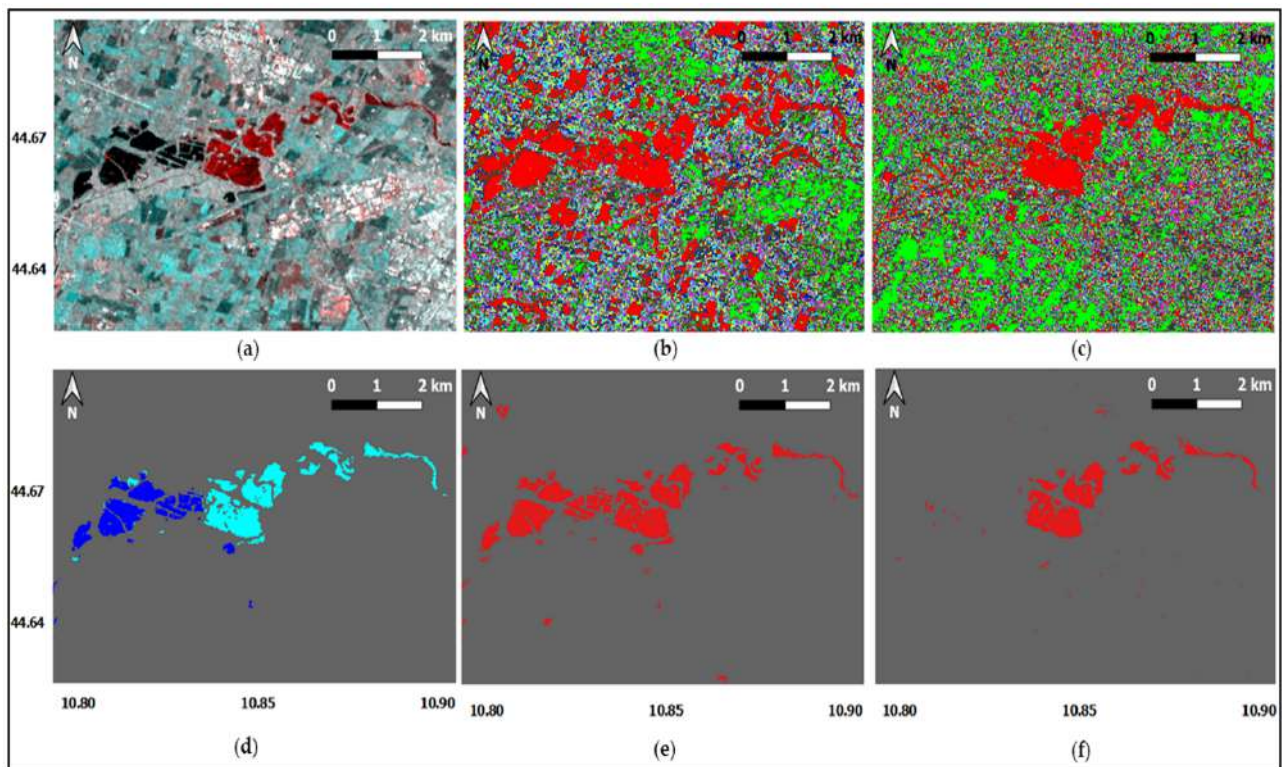


Figure 12. Full example of the results of the BFE approach implemented in AUTOWADE for the EMSR359 test case. Panel (a): RGB false color image produced using the S1 data (red: pre-flood image, green/blue: flood image); panel (b): output of the ISODATA applied to σ_{VV}^0 (CDWA in red); panel (c): output of the ISODATA applied to $\Delta\sigma_{VV}^0$ (CDEFA in red); panel (d): map of open floodwater (cyan)/permanent water (blue); panel (e): TDWA (in red); panel (f): TDEFA (in red). All the maps are zoomed on the area affected by the flood.

4.3. Accuracy Metrics and Extent of the Flooded Area

The results of the comparison between AUTOWADE-derived and CEMS-derived maps, expressed in terms of κ and F1-score, are reported in Table 5. The former metric is in the range [0.80–0.90] with an average value (over the 10 case studies) of 0.85, while the F1-score is in the range [0.87–0.94] with an average value of 0.90. Table 5 also includes the F1-score computed as the average of the F1-scores of the two water classes only. In this case, it ranges between 0.80 and 0.92 with an average value of 0.85. For what concerns the errors, they are reported in Table 6 for the class of permanent water and Table 7 for the class of open floodwater. Regarding $\varepsilon_{\text{comm}}$, it ranges between 0.6% and 21.4% with an average value (over the 10 case studies) of 9% for the class of permanent water, and between 8.5% and 25.3% with an average value of 17.5% for the class of open floodwater. For what concerns ε_{om} , it is in the range [2.5–32%] with an average value equal to 17.8% for permanent water, and in the range [1.7–21.2%] with an average value equal to 13.6% for floodwater.

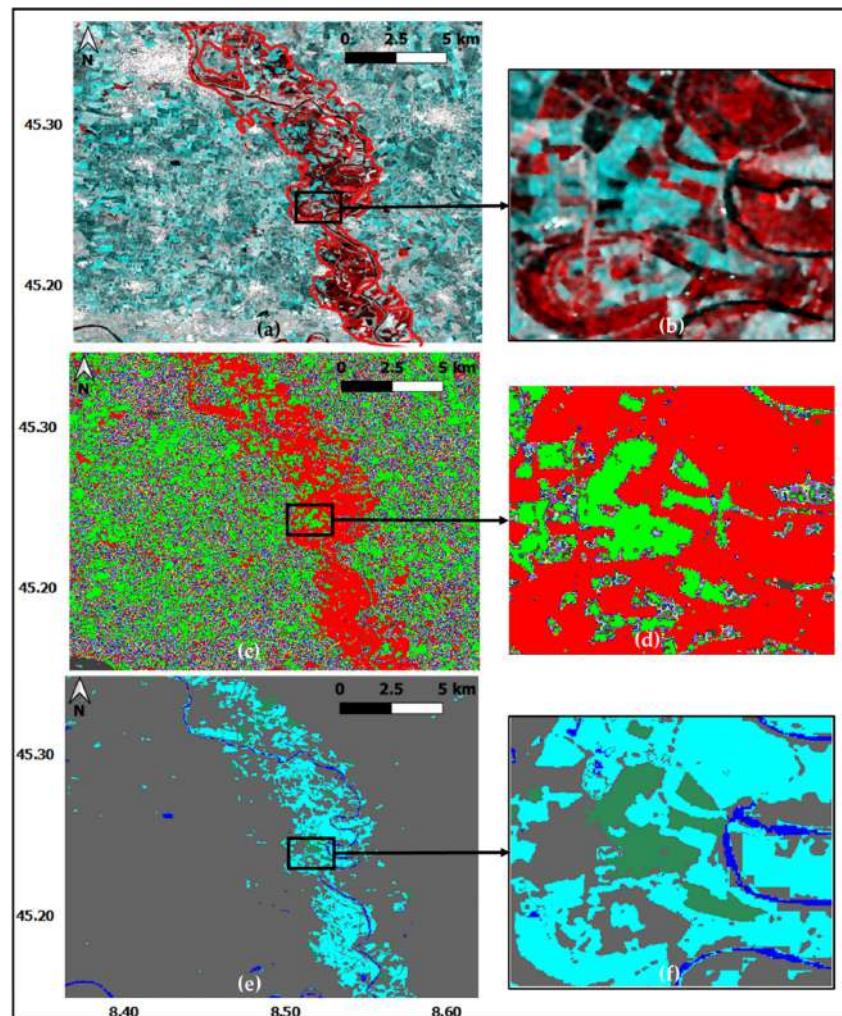


Figure 13. Example of the results of the method to map flooded vegetation implemented in AUTOWADE for the Vercelli test case. Panel (a): RGB false color image produced using the S1 data (red: pre-flood image, green/blue: flood image) with, superimposed in red, the boundaries of the flooded area detected using S2 data; panel (c): output of the ISODATA applied to $\Delta\sigma_{VV}^0$ (green: cluster of the objects with high $\Delta\sigma_{VV}^0$); panel (e): map of open floodwater (cyan), flooded vegetation (sea green) and permanent water (blue); panels (b,d,f): zooms on flooded vegetation.

Table 5. Comparison between CEMS-derived and AUTOWADE-derived open floodwater/permanent water maps in terms of kappa coefficient and F1-score. The latter has been computed as the arithmetic mean over individual F1-scores considering all the classes (3rd column), or only the two water classes (4th column).

CEMS Activation Code	κ	F1-Score	F1-score for Water Classes
EMSR359	0.87	0.91	0.87
EMSR411	0.84	0.90	0.85
EMSR417	0.90	0.91	0.86
EMSR429	0.84	0.90	0.85
EMSR437	0.80	0.88	0.83
EMSR445	0.87	0.90	0.86
EMSR492	0.84	0.87	0.80
EMSR496	0.87	0.94	0.92
EMSR501	0.83	0.89	0.84
EMSR502	0.86	0.89	0.84

Table 6. Commission and omission errors for the class of permanent water.

CEMS Activation Code	Commission Error [%]	Omission Error [%]
EMSR359	0.6	19.9
EMSR411	5.6	20.8
EMSR417	12.7	18.7
EMSR429	13.7	3.7
EMSR437	11.7	16.2
EMSR445	8.1	11.2
EMSR492	21.4	30.5
EMSR496	1.3	2.5
EMSR501	1.6	32.0
EMSR502	13.8	22.3

Table 7. Commission and omission errors for the class of open floodwater.

CEMS Activation Code	Commission Error [%]	Omission Error [%]
EMSR359	14.2	14.7
EMSR411	23.9	8.3
EMSR417	10.6	13.7
EMSR429	20.6	21.2
EMSR437	23.3	17.4
EMSR445	25.3	10.9
EMSR492	14.3	13.8
EMSR496	24.4	1.7
EMSR501	10.1	15.1
EMSR502	8.5	19.4

A second exercise has been carried out by calculating the errors for all the pixels included in the 10 areas of interest. The quite low values of the errors confirm the efficiency of AUTOWADE: $\epsilon_{\text{comm}} = 9.4\%$, $\epsilon_{\text{om}} = 25.6\%$, for permanent water and $\epsilon_{\text{comm}} = 14.8\%$, $\epsilon_{\text{om}} = 13.9\%$ for floodwater.

Table 8 reports, for each test case, the total extent of the flooded area estimated by CEMS and by AUTOWADE. The extent is expressed in ha and in percentage with respect to the size of the AOI.

Table 8. Comparison between CEMS-derived and AUTOWADE-derived open floodwater maps in terms of extent of the flooded area in ha and in percentage with respect to the size of the AOI (6th column of Table 2).

CEMS Activation Code	Total Flooded Surface Estimated by CEMS [ha]	Total Flooded Surface Estimated by AUTOWADE [ha]	Total Flooded Surface Estimated by CEMS [%]	Total Flooded Surface Estimated by AUTOWADE [%]
EMSR359	283	244	1.0	0.9
EMSR411	285	330	0.7	0.8
EMSR417	9460	8602	6.4	5.8
EMSR429	546	553	6.9	7.0
EMSR437	1850	1408	4.5	3.5
EMSR445	1358	1607	1.4	1.7
EMSR492	4899	4410	4.7	4.3
EMSR496	307	499	3.7	5.9
EMSR501	5039	4756	5.0	4.7
EMSR502	470	382	2.1	1.7

4.4. Delivery of the Flood/Permanent Water Map to the End User

After having processed all the tiles in which the S1 data acquired from one orbit are divided, the corresponding maps of flood/permanent water are resampled and reprojected to the reference spatial grid (Section 2.2). Then, they are mosaicked by merging them in one unique map, having pixel size of $20 \times 20 \text{ m}^2$, ready to be delivered to the end-user. By

performing the operations of resampling, reprojection, and mosaicking, the daily map of floodwater/permanent water on a national (Italian) scale is created and made available on a web-portal of the Italian DCP developed by CIMA Research Foundation named MyDewetra [50].

To make available the maps on MyDewetra, they are transformed in a vector file whose size in MB is considerably smaller than that of the original raster. This file is automatically delivered to MyDewetra to be visualized.

An example of how a daily map is presented to the end-user through MyDewetra is shown in Figure 14. Panel (a) shows what appears to the end-user when he/she opens MyDewetra and chooses a day of interest (9 December 2020, in this case, when a flood event affected Northern Italy). Panels (b) and (c) are two zooms on the areas mostly affected by the flood.

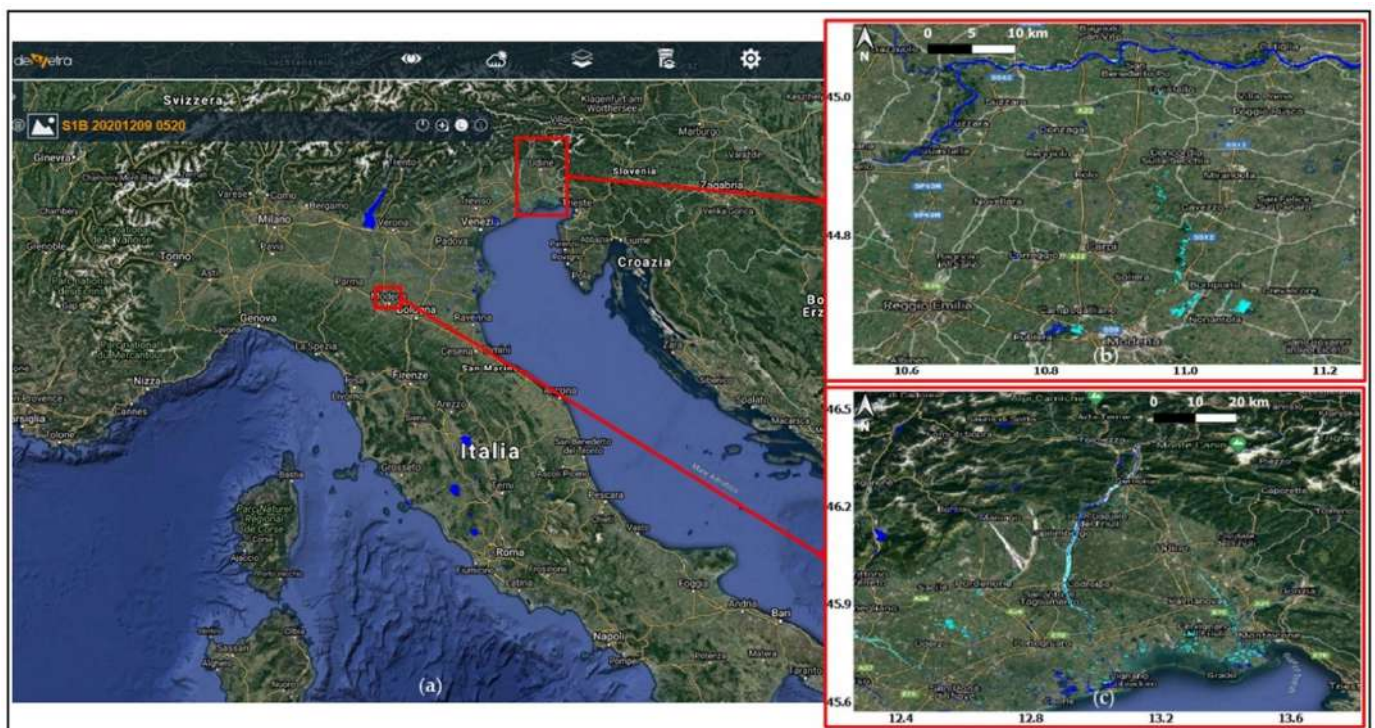


Figure 14. Typical AUTOWADE's output generated using the S1 acquisition performed on 9 December 2020 (orbit 95, the same considered to produce Figure 5). Panel (a) synoptic view; panels (b,c): zoom on two flooded areas. Blue: permanent water; cyan: floodwater.

5. Discussion

This paper presents the AUTOWADE tool, which has been conceived to provide the Italian DCP with a product that daily monitors floods and inland waters in a fully automatic way using S1 data. The service implemented by AUTOWADE is tested in pre-operational mode since early 2020 and has been extensively used to monitor the location and the extent of the floods that hit Italy in autumn 2020 (e.g., the events considered in Figures 13 and 14). AUTOWADE utilizes not only S1 data, but also S2 ones generated by a processor described in a previous paper [34], as well as ancillary data provided by the Copernicus Land Monitoring Service.

With respect to a previous paper dealing with an automated S1-based flood service [28], AUTOWADE monitors not only floods, but also permanent water bodies and searches for flooded vegetation in the gaps present in the open floodwater map. Moreover, it is tested on a quite large number of case studies.

With respect to previous studies on flood mapping from SAR data, this paper considers all the aspects related to the provision of an automated, national flood/water monitoring

product to an end-user, such as the automatic procurement of satellite data and the delivery of the product to the end-user. As for the algorithmic aspect, a new method is proposed, which does not use an image tile-based approach to determine a threshold that separates water from non-water, as commonly done in the literature (see the Introduction). The BFE approach implemented in AUTOWADE takes advantage of the availability of a reference water mask to identify the edges separating land from open water, also using a clustering method as the ISODATA. Focusing directly on the portion of a SAR image where standing water is present, instead of searching for it by iteratively dividing the image in tiles of different sizes, represents a simple method that improves computational efficiency. From this point of view, the application of a despeckling filter, performed in the preprocessing step, is the task with the higher computational burden, as pointed out also in [23], while neither the ISODATA, nor the histogram fitting are very time-consuming.

The combined use of an edge-filter and an automatic thresholding method was performed also in [51], where the filter was applied directly on a spectral index, derived from multispectral data, sensitive to the presence of water (Modified Normalized Difference Water Index [52]). In AUTOWADE, considering that SAR images are affected by speckle noise (despite of the application of a despeckling filter, some noise still remains in the images), it has been chosen to preliminarily use a clustering algorithm to make the data more immune to noise, as done in [53].

Regarding accuracy, for permanent water and open floodwater, it has been evaluated considering a set of test cases presenting large differences in terms of total flooded surface, ranging from 280 ha to 9460 ha (Table 2, last column and Table 8, 2nd column). Even the ratio between the flooded surface and the size of the AOI presents large differences ranging from less than 1% (EMSR411) to about 7% (EMSR429). The maximum discrepancy between CEMS-derived and AUTOWADE-derived maps in terms of total flooded surface is 858 ha (EMSR417; AUTOWADE: 8602 ha, CEMS: 9460 ha, see Table 8). However, in terms of percentage with respect to the size of the AOI, this discrepancy corresponds only to 0.6% (AUTOWADE: 5.8%, CEMS: 6.4%). The maximum percentage difference is 2.2% (EMSR496; AUTOWADE: 5.9%, CEMS: 3.7%).

Fairly good results have been obtained for all the case studies, especially considering κ and the F1-score. Almost equal values of the F1-score (0.90–0.91) have been obtained for the biggest flood (EMSR417) and the smallest ones (EMSR359–411). The same applies considering the F1-score computed as the average of the F1-scores of the two water classes only (0.85–0.87).

As for the errors of omission and commission, even better results were obtained in the literature (e.g., [23,31,54]), but it must be considered that in this study, 3 classes are considered, while in previous studies, only non-water and floodwater were generally distinguished. It has been found that the major source of disagreement between AUTOWADE-derived maps and reference maps is the misclassification between permanent water and floodwater. On the one hand, this happens because CEMS does not use a pre-flood image, while AUTOWADE labels as permanent water the pixels classified as open water in the flood image and in the pre-flood one. On the other hand, the misclassification is also due to differences between the hydrography data included in the CEMS products and the reference water mask. This has nothing to do with the accuracy of the AUTOWADE-derived maps.

For what concerns permanent water, the high value of ε_{om} obtained for the EMSR492 case study (30.5%, Table 6) is mostly due to a small water course whose delineation with S1 was partially hampered by the presence of many mixed land-water pixels (data with higher spatial resolution would have been necessary for a more precise delineation). The high value of ε_{om} obtained for the EMSR501 case study (32%, Table 6) is mostly due to a water body (Drin River) whose detection was missed because of unexpected high values of backscattering likely due to the presence of wind blowing above the water surface.

The extent of the objects labelled as open floodwater is the major cause of misclassification between open floodwater and non-water. An example of this kind of misclassification

is shown in Figure 15 for the Springfield Clonara test site (EMSR429). For the class of open floodwater, ϵ_{comm} and ϵ_{om} are equal to about 20%, in this case. Looking at Figure 15, it can be seen that, although there is a substantial agreement between CEMS and AUTOWADE classifications, the size of the floodwater objects is slightly different. This is due to the differences in the flood detection methods; in particular, the BFE approach uses RG and uncertainties in the determination of the tolerance of the RG may imply uncertainties in the extent of the floodwater objects. The red pixels in the lower left part of Figure 15 correspond to omission errors due to small differences between the σ^0 values measured by S1 under non-flooded and flooded conditions, considering that the BFE approach applies change detection. Note that for this test case commission and omission errors are of the same order of magnitude (around 20%); thus, the difference between the total flooded surface estimated by CEMS and that estimated by AUTOWADE is quite small (7 ha, Table 8).

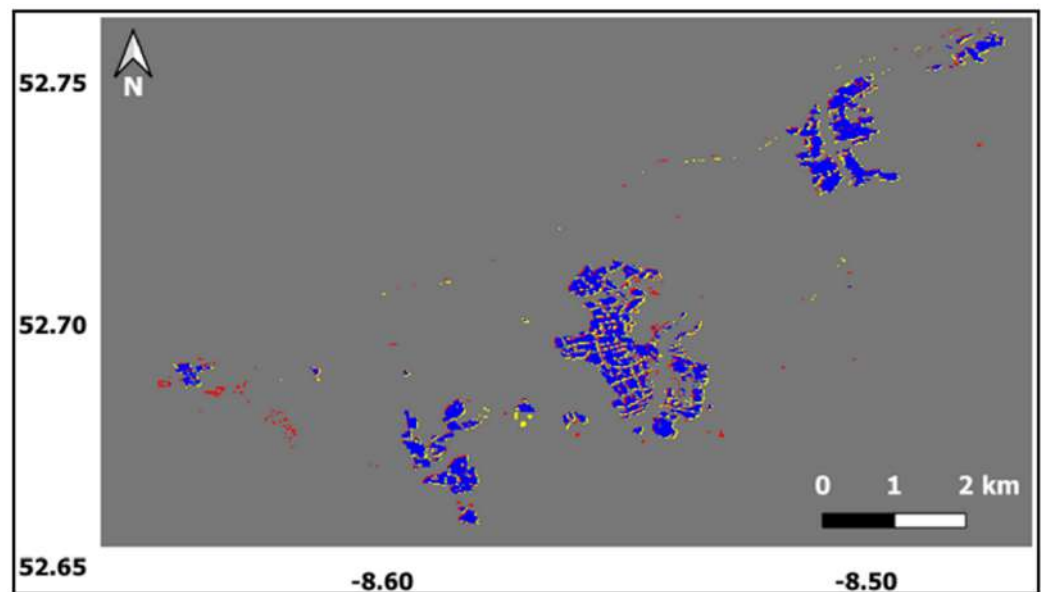


Figure 15. Areas classified as open floodwater by AUTOWADE and CEMS for the Springfield Clonara case study (EMSR 429). Blue: floodwater in both CEMS-derived and AUTOWADE-derived maps; red: floodwater only in the CEMS-derived map; yellow floodwater only in the AUTOWADE-derived map.

Thanks to the availability of some aerial photos, it has been verified that the quite high value of ϵ_{comm} obtained for the EMSR496 case study (24.4%, class of open floodwater), is due to the presence of ponding water not detected by CEMS. This can be inferred by looking at Figure 16 that compares the maps with two photos of the area affected by the flood. In the areas highlighted by the ellipses, CEMS seems to underestimate water, while in the AUTOWADE-derived map, the underestimation is significantly reduced (especially in the magenta ellipse). The photos were taken on 26 January 2021 at 11:00 UTC, i.e., about 17 h before the S1 acquisition, but, reportedly, water did not recede. Hence, the disagreement with respect to the reference data in terms of ratio between the extent of the flooded area and the size of the AOI highlighted above for this case study (2.2%) is probably not due to an overestimation of the flooded area done by AUTOWADE.

It was not possible to robustly validate the method designed to map flooded vegetation, because CEMS products do not map this target when they are derived from SAR data. Nonetheless, by comparing the AUTOWADE-derived map with that derived from a S2 image acquired on the same day, it has been found that the image objects marked as flooded vegetation allowed us to fill some gaps present in the floodwater map that are not realistic from a hydrological point of view (Vercelli test case, Figure 13f), because the area affected by the flood has a quite uniform surface elevation. Several gaps are still present in the map and it is likely that flooded vegetation is underestimated. However,

it must be considered that, when dense vegetation is present, SAR is not sensitive to the presence of floodwater beneath the canopy (we remind again that pixels with $NDVI > 0.7$ are masked by AUTOWADE). Moreover, double bounce is the prevailing effect caused by flooded vegetation for stem-dominated vegetation, while, for leaf-dominated vegetation, volume scattering generally prevails [12] and surface water detection is complicated. Even in Figure 16, the presence of flooded vegetation is evident (red ellipse in panel d); while this target is not detected by the CEMS-derived map, in the AUTOWADE derived map the presence of gaps is reduced, and the area highlighted by the red ellipses is correctly labelled as flooded vegetation.

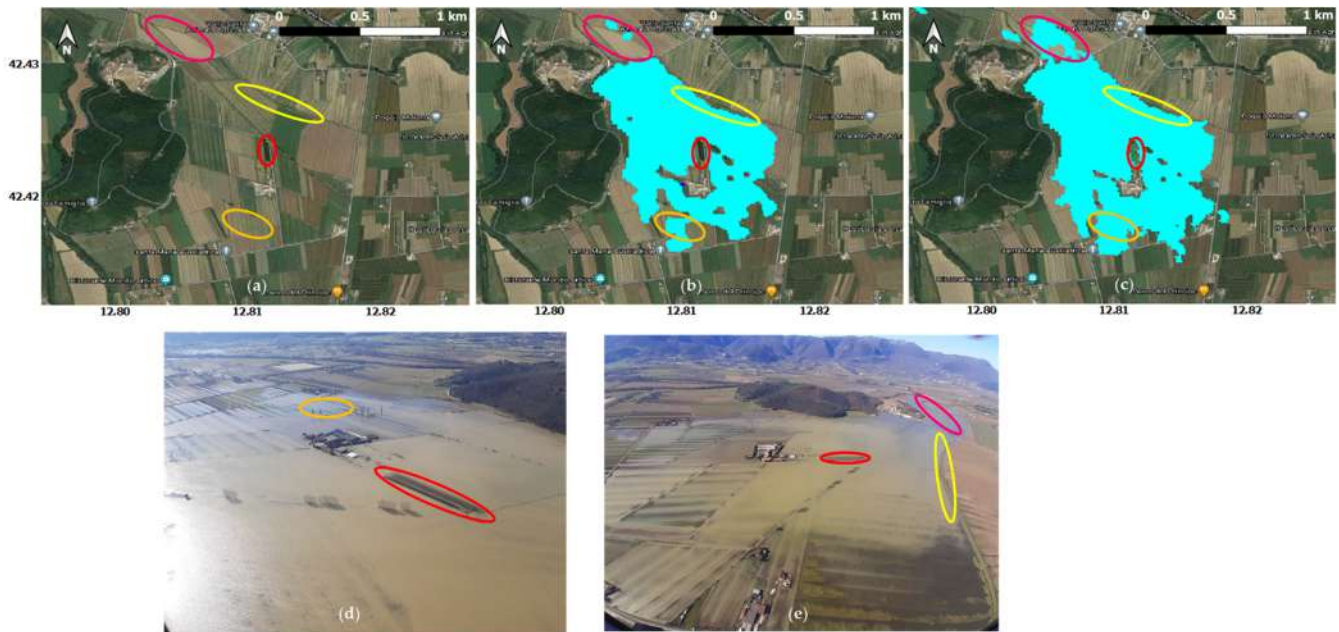


Figure 16. Comparison, for the Rieti flood (EMSR496), among the CEMS-derived map (panel b), the AUTOWADE-derived map (panel c), and a couple of aerial photos taken on 26 January 2021, at 11:00 UTC (d,e). Panel (a) is the reference Google-Hybrid map. Same colors of the ellipses correspond to the same zone in the maps and the photos. In panels (b,c), cyan represents open floodwater; in panel (c), sea-green represents flooded vegetation.

Flooded vegetation mapping builds on the results of a previous study regarding the combined use of VV and VH polarizations [47] (confirmed in [11,48]), based on the consideration that the dihedral effect, generated by an horizontal surface (water) and a vertical one (plants' stems), keeps the same polarization throughout the radar scattering path. Note that it has been demonstrated that in the presence of slanted vegetation, the double bounce scattering also generates a cross-polarized signal [55]. However, plants having a slanted root structure like saltwater mangroves are typical of tropical areas rather than temperate ones like Italy.

The major limitation of AUTOWADE and of the BFE method implemented in AUTOWADE to map open water is related to the processing of a S1 frame where big water bodies are missing, and a reference water mask cannot be derived. In this case, the MCDWA cannot be created from the CDWA. This problem can be at least partially overcome using the edge between the original CDWA and the other areas to identify, through the buffer zones created around it, a subset of image pixels characterized by a bimodal histogram (as done in [35]). Although AUTOWADE has been conceived to work on a national (Italian) scale, the results of the validation (Section 4.3) demonstrate that the BFE can be applied in other European countries. In principle, nothing prevents a user from applying the BFE method outside Europe, but the reference mask derived from the WAW product is currently available only for Europe.

The other constraints are related to the SAR ability to detect water in some landscapes, like areas of high relief or dense vegetation and to the possibility to confuse some targets like melting snow, frozen soil, or desert areas with water surfaces. These constraints are common to any automatic algorithm that does not use any amount of supervision. However, the presence of water is very unlikely in steep slope areas. Moreover, melting snow is mapped using ancillary S2 data if cloud cover does not hamper snow detection, whereas desert areas are not present in Italy.

The use of a buffer zone of fixed buffering distance (1 km), done to classify pixels belonging only to the TDWA/TDFA and not to the CDWA/CDFA (Sections 3.2.2 and 3.2.3), can be considered as a critical aspect, because the choice of 1 km, done based on our previous experience with SAR images of inundations, is subjective and may be questioned. However, this situation generally regards a few pixels (often forming objects smaller than the minimum mapping unit), as demonstrated in Figure 12, and does not have a significant impact on the final map.

6. Conclusions

The AUTOWADE tool designed for a fully automated service of floodwater/permanent water mapping using Sentinel-1 data has been presented. Although several studies available in the literature dealt with the problem of flood mapping using SAR data, the creation of a processing chain that automates the various steps needed to set up an operational service was rarely tackled. These steps include not only the processing of the SAR images, but also the data procurement and the delivery of the maps to the end-user.

The service implemented by AUTOWADE daily generates a map of floodwater/permanent water on a national scale (Italy) with a spatial resolution of $20 \times 20 \text{ m}^2$ in order to provide the Italian Department of Civil Protection with a systematic detection and monitoring of any event occurring in Italy without requiring any activation. For a given location, the average revisit frequency of the maps is 2–3 days (considering both ascending and descending orbits and orbit overlap). AUTOWADE has been tested in fully pre-operational mode since early 2020. Its daily products are automatically delivered to the Italian Department of Civil Protection and can be visualized through a web portal.

AUTOWADE includes an algorithm to map open water, based on the new buffer-form-edge (BFE) approach. The BFE approach combines different techniques such as clustering, edge filtering, thresholding, and region growing. Nonetheless, it is quite simple in computation and effective in identifying bare/scarcely vegetated surfaces covered by water. It is therefore suitable for real-time applications, especially if a large amount of SAR data has to be processed, as necessary for a service working on a national scale. The comparison with maps produced by the Copernicus Emergency Management Service has shown that the BFE approach performs quite well. Moreover, vegetated areas adjacent to those classified as flooded are analyzed in order to fill a portion of the gaps present in the maps likely due to undetected flooded vegetation.

Future work will concern the inclusion in the AUTOWADE-derived product of an evaluation of the classification uncertainty. An uncertainty map complementing the water map will be made available to the end user. Moreover, future releases of AUTOWADE will take advantage of more accurate ancillary data, such as the Copernicus DEM and a refined land cover map obtained by complementing the Corine Land Cover product with data provided by the Global Human Settlement Layer to better identify urban areas.

Author Contributions: Conceptualization, L.P., G.S., and S.P.; methodology, L.P., G.S., and E.F.; software, L.P. and G.S.; validation, L.P.; formal analysis, L.P.; investigation, L.P.; resources, L.F.; data curation, G.S., E.F., and L.P.; writing—original draft preparation, L.P., G.S., and E.F.; writing—review and editing, L.P., G.S., E.F., L.F., and S.P.; visualization, G.S., E.F., and L.P.; supervision, S.P.; project administration, L.F.; funding acquisition, L.F. All authors have read and agreed to the published version of the manuscript.

Funding: This research was funded by the Italian Department of Civil Protection, Presidency of the Council of Ministers, through the convention between Department of Civil Protection and CIMA Research Foundation, for the development of knowledge, methodologies, technologies, and training, useful for the implementation of national systems of monitoring, prevention, and surveillance.

Institutional Review Board Statement: Not applicable.

Informed Consent Statement: Not applicable.

Data Availability Statement: Sentinel-1 data are available at <https://scihub.copernicus.eu/dhus/#/home> (accessed on 31 March 2021).

Acknowledgments: L.P. acknowledges support from the E-SHAPE project, funded by the European Union's Horizon 2020 Research and Innovation Programme under grant agreement No. 820852. The photographs of the area hit by the flood occurred in the Rieti district in January 2021 were taken by the staff of the Lazio region.

Conflicts of Interest: The authors declare no conflict of interest.

Appendix A. The ISODATA

The ISODATA is an unsupervised clustering algorithm that separates groups of objects in a scene. A typical scene consists of regular and/or irregular regions arranged in a patchwork manner, each containing one class of surface cover type (e.g., flooded areas, croplands, forests, manmade structures, etc.); these homogeneous regions are the objects in the scene. Objects within each cluster should be as close to each other as possible and as far from other objects in other clusters as possible. The ISODATA begins with arbitrary cluster means and then clusters the pixels according to the minimum spectral distance technique. It is an iterative procedure, in which each iteration recalculates means and reclassifies pixels with respect to the new means. The process ends when a maximum number of iterations has been performed, or a maximum percentage of unchanged pixels between two iterations has been reached. The ISODATA does not keep a fixed number of clusters. In particular, clusters having a very large number of members are split, while if two cluster means are very close in terms of spectral distance (e.g., they represent an unnecessary or an injudicious division of the data), they are merged [38]. Clusters that contain so few points as to be meaningless (e.g., that they would not give acceptable statistics estimates if used in training a maximum likelihood classifier) are discarded and their members are reassigned to other clusters.

Since the ISODATA splits and merges clusters, it just requires specifying a range for the number of clusters. The optimum number of clusters is not known, so it is generally chosen to be conservatively high [38].

Appendix B. Bimodality Check

AUTOWADE checks the bimodality of the histogram of the pixel values by evaluating the Ashman's D coefficient [43], the bimodality coefficient [44,45], and the ratio between the modes of the distribution.

The Ashman's D coefficient quantifies how well two Gaussian distributions are separated, thus assuming a Gaussian mixture model for the distribution of the corresponding populations. It is defined as [56]:

$$D = \sqrt{2} \frac{|\mu_1 - \mu_2|}{\sqrt{\sigma_1^2 + \sigma_2^2}} \quad (\text{A1})$$

where μ_1 and μ_2 are the mean values of the distributions and σ_1 and σ_2 are the corresponding standard deviations. A distribution has two peaks if $D > 2$.

The bimodality coefficient is defined as:

$$BC = \frac{\gamma^2 + 1}{k + \frac{3(P-1)^2}{(P-2)(P-3)}} \quad (A2)$$

where P is the population size, k is the kurtosis, and γ is the skewness of the distribution. Values of BC greater than $5/9$ (~ 0.555) indicate a bimodal distribution.

A further check assumes that a minimum percentage of the total data should be in each mode of a bimodal distribution. This constraint is made explicit by introducing the weight ratio defined as [56]:

$$W = \min_{i,j} \left(\frac{M_i}{M_j} \right) \quad i, j = 1 : 2 \quad (A3)$$

where $M_{i,j}$ are the modes of the distributions.

The bimodality test is assumed as passed if $D > 2$ [43], $W > 0.2$ (each mode should contain at least 10% of the total population of pixels), $BC > 0.4$. Note that a conservative choice has been done for W because in [24,56] a value of 0.1 is suggested. Conversely, although a threshold value of $5/9$ is commonly suggested for BC (corresponding to the value of BC for a uniform distribution), this constraint has been relaxed considering that a Gaussian mixture model has been assumed and that the value of BC for a Gaussian distribution is around 0.33. Note that D , W and BC are evaluated considering the Gaussian functions fitting the histograms of water/flooded and non-water/non-flooded pixels (Section 3.2.2).

Appendix C. Fuzzy Logic

The fuzzy sets basically represent an extension of the classical notion of set. While in classical set theory, an element either belongs or does not belong to the set, elements of a fuzzy set have degrees of membership. The degrees are defined through membership functions whose values are real numbers in the interval $[0, 1]$. The application of the membership functions represents the so-called fuzzification, which in AUTOWADE is simply performed using the S membership function shown in one of the boxes of Figure 11 and defined as $S(x, x_1, x_2)$ where x is the independent variable and x_1, x_2 are the parameters of the function. For $x \leq x_1$, $S = 0$, while for $x \geq x_2$, $S = 1$. For x values within the interval between x_1 and x_2 , the membership degree depends on the position in the interval itself. Note that an object-based application of the fuzzy logic is performed by AUTOWADE (Section 3.2.4).

The final operation of any fuzzy-based approach is the defuzzification that assigns each element of a fuzzy set to a class, according to the final membership degree. In AUTOWADE, the final membership degree is computed as the average of the degrees resulting from the application of the S function to $\Delta\sigma_{VV}^0$, $\Delta\sigma_{VV}^0 - \Delta\sigma_{VH}^0$ and p (Section 3.2.4). A simple threshold-based defuzzification is carried out by labelling a flooded vegetation an object whose final membership degree is larger than 0.5.

References

1. Peters, E.; Bier, G.; van Lanen, H.A.J.; Torfs, P.J.J.F. Propagation and spatial distribution of drought in a groundwater catchment. *J. Hydrol.* **2006**, *321*, 257–275. [CrossRef]
2. Shen, X.; Wang, D.; Mao, K.; Anagnostou, E.; Hong, Y. Inundation extent mapping by synthetic aperture radar: A review. *Remote Sens.* **2019**, *11*, 879. [CrossRef]
3. Pulvirenti, L.; Pierdicca, N.; Chini, M.; Guerriero, L. An algorithm for operational flood mapping from Synthetic Aperture Radar (SAR) data using fuzzy logic. *Nat. Hazards Earth Syst. Sci.* **2011**, *11*, 529–540. [CrossRef]
4. Matgen, P.; Hostache, R.; Schumann, G.; Pfister, L.; Hoffmann, L.; Savenije, H.H.G. Towards an automated SAR-based flood monitoring system: Lessons learned from two case studies. *Phys. Chem. Earth* **2011**, *36*, 241–252. [CrossRef]
5. Martinis, S.; Twele, A.; Voigt, S. Towards operational near real-time flood detection using a split-based automatic thresholding procedure on high resolution TerraSAR-X data. *Nat. Hazards Earth Syst. Sci.* **2009**, *9*, 303–314. [CrossRef]

6. Moya, L.; Endo, Y.; Okada, G.; Koshimura, S.; Mas, E. Drawback in the change detection approach: False detection during the 2018 western Japan floods. *Remote Sens.* **2019**, *11*, 2320. [[CrossRef](#)]
7. Pierdicca, N.; Pulvirenti, L.; Chini, M.; Guerriero, L.; Candela, L. Observing floods from space: Experience gained from COSMO-SkyMed observations. *Acta Astronaut.* **2013**, *84*, 122–133. [[CrossRef](#)]
8. Pulvirenti, L.; Chini, M.; Pierdicca, N.; Boni, G. Use of SAR data for detecting floodwater in urban and agricultural areas: The role of the interferometric coherence. *IEEE Trans. Geosci. Remote Sens.* **2016**, *54*, 1532–1544. [[CrossRef](#)]
9. Pulvirenti, L.; Pierdicca, N.; Chini, M.; Guerriero, L. Monitoring Flood Evolution in Agricultural Areas Using COSMO-SkyMed data: Analysis of the Tuscany inundation of December 2009. In *SAR Image Analysis, Modeling, and Techniques XI*; International Society for Optics and Photonics: San Francisco, CA, USA, 2011; Volume 8179.
10. Pulvirenti, L.; Pierdicca, N.; Chini, M.; Guerriero, L. Monitoring flood evolution in vegetated areas using cosmo-skymed data: The tuscany 2009 case study. *IEEE J. Sel. Top. Appl. Earth Obs. Remote Sens.* **2013**, *6*, 1807–1816. [[CrossRef](#)]
11. Tsyganskaya, V.; Martinis, S.; Marzahn, P. Flood monitoring in vegetated areas using multitemporal Sentinel-1 data: Impact of time series features. *Water* **2019**, *11*, 1938. [[CrossRef](#)]
12. Pierdicca, N.; Pulvirenti, L.; Boni, G.; Squicciarino, G.; Chini, M. Mapping Flooded Vegetation Using COSMO-SkyMed: Comparison With Polarimetric and Optical Data Over Rice Fields. *IEEE J. Sel. Top. Appl. Earth Obs. Remote Sens.* **2017**, *10*, 2650–2662. [[CrossRef](#)]
13. Refice, A.; Zingaro, M.; D’addabbo, A.; Chini, M. Integrating C-and L-band SAR imagery for detailed flood monitoring of remote vegetated areas. *Water* **2020**, *12*, 2745. [[CrossRef](#)]
14. Mason, D.C.; Dance, S.L.; Vetra-Carvalho, S.; Cloke, H.L. Robust algorithm for detecting floodwater in urban areas using synthetic aperture radar images. *J. Appl. Remote Sens.* **2018**, *12*, 045011. [[CrossRef](#)]
15. Chini, M.; Pelich, R.; Pulvirenti, L.; Pierdicca, N.; Hostache, R.; Matgen, P. Sentinel-1 InSAR Coherence to Detect Floodwater in Urban Areas: Houston and Hurricane Harvey as A Test Case. *Remote Sens.* **2019**, *11*, 107. [[CrossRef](#)]
16. Pulvirenti, L.; Chini, M.; Pierdicca, N. InSAR Multitemporal Data over Persistent Scatterers to Detect Floodwater in Urban Areas: A Case Study in Beletweyne, Somalia. *Remote Sens.* **2021**, *13*, 37.
17. D’Addabbo, A.; Refice, A.; Pasquariello, G.; Lovergine, F.P.; Capolongo, D.; Manfreda, S. A Bayesian Network for Flood Detection Combining SAR Imagery and Ancillary Data. *IEEE Trans. Geosci. Remote Sens.* **2016**, *54*, 3612–3625. [[CrossRef](#)]
18. Pulvirenti, L.; Marzano, F.S.; Pierdicca, N.; Mori, S.; Chini, M. Discrimination of water surfaces, heavy rainfall, and wet snow using COSMO-SkyMed observations of severe weather events. *IEEE Trans. Geosci. Remote Sens.* **2014**, *52*, 858–869. [[CrossRef](#)]
19. Vespe, F.; Baldini, L.; Notarnicola, C.; Prati, C.; Zerbini, S.; Celidonio, G. Integration of X-SAR observations with data of other remote sensing techniques: Preliminary results achieved with Cosmo/SkyMed announcement of opportunity projects. In *SAR Image Analysis, Modeling, and Techniques XI*; International Society for Optics and Photonics: Washington, DC, USA, 2011; Volume 8179, p. 817907.
20. Baldini, L.; Roberto, N.; Gorgucci, E.; Fritz, J.; Chandrasekar, V. Analysis of precipitation in repeated acquisitions collected by the COSMO SkyMed constellation in polarimetric mode. In Proceedings of the International Geoscience and Remote Sensing Symposium (IGARSS), Vancouver, BC, Canada, 24–29 July 2011; pp. 2349–2352.
21. Baldini, L.; Roberto, N.; Gorgucci, E.; Facheris, L.; Chandrasekar, V. Effects of precipitation on images collected using different operational modes of Cosmo Sky Med. In Proceedings of the International Geoscience and Remote Sensing Symposium (IGARSS), Munich, Germany, 22–27 July 2012; pp. 2403–2406.
22. Clement, M.A.; Kilsby, C.G.; Moore, P. Multi-temporal synthetic aperture radar flood mapping using change detection. *J. Flood Risk Manag.* **2018**, *11*, 152–168. [[CrossRef](#)]
23. Amitrano, D.; Di Martino, G.; Iodice, A.; Riccio, D.; Ruello, G. Unsupervised Rapid Flood Mapping Using Sentinel-1 GRD SAR Images. *IEEE Trans. Geosci. Remote Sens.* **2018**, *56*, 3290–3299. [[CrossRef](#)]
24. Chini, M.; Hostache, R.; Giustarini, L.; Matgen, P. A hierarchical split-based approach for parametric thresholding of SAR images: Flood inundation as a test case. *IEEE Trans. Geosci. Remote Sens.* **2017**, *55*, 6975–6988. [[CrossRef](#)]
25. Martinis, S.; Kersten, J.; Twele, A. A fully automated TerraSAR-X based flood service. *ISPRS J. Photogramm. Remote Sens.* **2015**, *104*, 203–212. [[CrossRef](#)]
26. Boni, G.; Ferraris, L.; Pulvirenti, L.; Squicciarino, G.; Pierdicca, N.; Candela, L.; Pisani, A.R.; Zoffoli, S.; Onori, R.; Proietti, C.; et al. A Prototype System for Flood Monitoring Based on Flood Forecast Combined with COSMO-SkyMed and Sentinel-1 Data. *IEEE J. Sel. Top. Appl. Earth Obs. Remote Sens.* **2016**, *9*, 2794–2805. [[CrossRef](#)]
27. Tholey, N.; Clandillon, S.; Luzietti, L.; Maxant, J.; Battiston, S.; Yesou, H. Exploitation of Sentinel-1 Data for Flood Mapping and Monitoring within the Framework of the Copernicus Emergency Core and Downstream Services. In Proceedings of the International Geoscience and Remote Sensing Symposium (IGARSS), Yokohama, Japan, 28 July–2 August 2019; pp. 5393–5396.
28. Twele, A.; Cao, W.; Plank, S.; Martinis, S. Sentinel-1-based flood mapping: A fully automated processing chain. *Int. J. Remote Sens.* **2016**, *37*, 2990–3004. [[CrossRef](#)]
29. Bovolo, F.; Bruzzone, L. A Split-Based Approach to Unsupervised Change Detection in Large-Size Multitemporal Images: Application to Tsunami-Damage Assessment. *IEEE Trans. Geosci. Remote Sens.* **2007**, *45*, 1658–1669. [[CrossRef](#)]
30. Martinis, S.; Twele, A.; Voigt, S. Unsupervised extraction of flood-induced backscatter changes in SAR data using markov image modeling on irregular graphs. *IEEE Trans. Geosci. Remote Sens.* **2011**, *49*, 251–263. [[CrossRef](#)]

31. Cao, H.; Zhang, H.; Wang, C.; Zhang, B. Operational flood detection using Sentinel-1 SAR data over large areas. *Water (Switzerland)* **2019**, *11*, 786. [[CrossRef](#)]
32. Yamazaki, D.; Ikeshima, D.; Tawatari, R.; Yamaguchi, T.; O'Loughlin, F.; Neal, J.C.; Sampson, C.C.; Kanae, S.; Bates, P.D. A high-accuracy map of global terrain elevations. *Geophys. Res. Lett.* **2017**, *44*, 5844–5853. [[CrossRef](#)]
33. Company General Use GMES Initial Operations/Copernicus Land Monitoring Services-Validation of products HRL Water and Wetness 2015 Final Validation Report. 2019. Available online: <https://land.copernicus.eu/user-corner/technical-library/hrl-water-and-wetness-2015-validation-report> (accessed on 5 March 2021).
34. Pulvirenti, L.; Squicciarino, G.; Fiori, E.; Fiorucci, P.; Ferraris, L.; Negro, D.; Gollini, A.; Severino, M.; Puca, S. An automatic processing chain for near real-time mapping of burned forest areas using Sentinel-2 data. *Remote Sens.* **2020**, *12*, 674. [[CrossRef](#)]
35. Pulvirenti, L.; Squicciarino, G.; Fiori, E. A method to automatically detect changes in multitemporal spectral indices: Application to natural disaster damage assessment. *Remote Sens.* **2020**, *12*, 2681. [[CrossRef](#)]
36. Ulaby, F.T.; Dobson, M.C. *Handbook of Radar Scattering Statistics for Terrain*; Artech House: Norwood, MA, USA, 1989; Volume 1, ISBN 0890063362.
37. Lopes, A.; Touzi, R.; Nezry, E. Adaptive Speckle Filters and Scene Heterogeneity. *IEEE Trans. Geosci. Remote Sens.* **1990**, *28*, 992–1000. [[CrossRef](#)]
38. Richards, J.A.; Jia, X. *Remote sensing digital image analysis: An introduction*; Esa/Esrin: Frascati, Italy, 2006; ISBN 3540251286.
39. Davis, L.S. A survey of edge detection techniques. *Comput. Graph. Image Process.* **1975**, *4*, 248–270. [[CrossRef](#)]
40. Otsu, N. A Threshold Selection Method from Gray Level Histograms. *IEEE Trans. Syst. Man. Cybern.* **1979**, *9*, 62–66. [[CrossRef](#)]
41. Haralick, R.M.; Shapiro, L.G. Survey: Image Segmentation Techniques. *Int. J. Future Comput. Commun.* **2014**, *3*, 89.
42. Adams, R.; Bischof, L. Seeded Region Growing. *IEEE Trans. Pattern Anal. Mach. Intell.* **1994**, *16*, 641–647. [[CrossRef](#)]
43. Ashman, K.A.; Bird, C.M.; Zepf, S.E. Detecting bimodality in astronomical datasets. *Astron. J.* **1994**, *108*, 2348–2361. [[CrossRef](#)]
44. Guide, S.A.S.U. *SAS/STAT User's Guide. Version 6*; SAS Institute Incorporated: Cary, NC, USA, 1990.
45. Pfister, R.; Schwarz, K.A.; Janczyk, M.; Dale, R.; Freeman, J.B. Good things peak in pairs: A note on the bimodality coefficient. *Front. Psychol.* **2013**, *4*, 700. [[CrossRef](#)] [[PubMed](#)]
46. Giustarini, L.; Hostache, R.; Matgen, P.; Schumann, G.-P.; Bates, P.D.; Mason, D.C. A change detection approach to flood mapping in urban areas using TerraSAR-X. *Geosci. Remote Sens. IEEE Trans.* **2013**, *51*, 2417–2430. [[CrossRef](#)]
47. Chini, M.; Papastergios, A.; Pulvirenti, L.; Pierdicca, N.; Matgen, P.; Parcharidis, I. SAR coherence and polarimetric information for improving flood mapping. In Proceedings of the International Geoscience and Remote Sensing Symposium (IGARSS), Beijing, China, 10–15 July 2016.
48. Tsyganskaya, V.; Martinis, S.; Marzahn, P.; Ludwig, R. Detection of temporary flooded vegetation using Sentinel-1 time series data. *Remote Sens.* **2018**, *10*, 1286. [[CrossRef](#)]
49. Opitz, J.; Burst, S. Macro F1 and Macro F1. *arXiv* **2019**, arXiv:1911.03347.
50. Pagliara, P.; Corina, A.; Burastero, A.; Campanella, P.; Ferraris, L.; Morando, M.; Rebora, N.; Versace, C. Dewetra, coping with emergencies. In Proceedings of the 8th International ISCRAM Conference, Lisbon, Portugal, 8–11 May 2011.
51. Donchyts, G.; Schellekens, J.; Winsemius, H.; Eisemann, E.; van de Giesen, N. A 30 m resolution surfacewater mask including estimation of positional and thematic differences using landsat 8, SRTM and OpenStreetMap: A case study in the Murray-Darling basin, Australia. *Remote Sens.* **2016**, *8*, 386. [[CrossRef](#)]
52. Xu, H. Modification of normalised difference water index (NDWI) to enhance open water features in remotely sensed imagery. *Int. J. Remote Sens.* **2006**, *27*, 3025–3033. [[CrossRef](#)]
53. Pulvirenti, L.; Chini, M.; Pierdicca, N.; Guerriero, L.; Ferrazzoli, P. Flood monitoring using multi-temporal COSMO-skymed data: Image segmentation and signature interpretation. *Remote Sens. Environ.* **2011**, *115*, 990–1002. [[CrossRef](#)]
54. Li, Y.; Martinis, S.; Plank, S.; Ludwig, R. An automatic change detection approach for rapid flood mapping in Sentinel-1 SAR data. *Int. J. Appl. Earth Obs. Geoinf.* **2018**, *73*, 123–135. [[CrossRef](#)]
55. Hong, S.H.; Wdowinski, S. Double-bounce component in cross-polarimetric SAR from a new scattering target decomposition. *IEEE Trans. Geosci. Remote Sens.* **2014**, *52*, 3039–3051. [[CrossRef](#)]
56. Vilasa, L.; Miralles, D.G.; De Jeu, R.A.M.; Dolman, A.J. Global soil moisture bimodality in satellite observations and climate models. *J. Geophys. Res. Atmos.* **2017**, *122*, 4299–4311. [[CrossRef](#)]